The Pennsylvania State University

The Graduate School

College of Earth and Mineral Sciences

TOPOGRAPHICALLY DRIVEN GROUNDWATER FLOW THROUGH A HETEROGENEOUS PERMEABILITY SUBSURFACE: IMPLICATIONS FOR SURFACE HEAT FLOW NEAR PARKFIELD, CALIFORNIA AND IN THE WESTERN MOJAVE DESERT

A Thesis in

Geosciences

by

Margaret A. Popek

Submitted in Partial Fulfillment

of the Requirements

for the Degree of

Master of Science

December 2009

The thesis of Margaret A. Popek was reviewed and approved* by the following:

Demian M. Saffer

Associate Professor of Geosciences

Thesis Adviser

Kamini Singha

Assistant Professor of Geosciences

Richard R. Parizek

Professor of Geosciences and Geo-Environmental Engineering

Katherine H. Freeman

Associate Department Head of Graduate Programs and Professor, Department of Geosciences

* Signatures are on file in the Graduate School.

ABSTRACT

Surface heat flow in the California Coast Ranges near Parkfield, CA exhibits substantial scatter, with differences as large 20 mW/m^2 over lateral distances of 5-70 km. In contrast, surface heat flow in many other parts of the California dataset displays only an ~ 10 mW/m^2 range. This scatter in surface heat flow near Parkfield has been an important limitation on interpretations of geodynamic processes, but to date has not been explained. Here, I use a numerical model of coupled fluid and heat transport to test the hypothesis that heat advection by groundwater flow through an upper crust characterized by heterogeneous permeability can generate the magnitude and spatial characteristics of the scatter in the Parkfield heat flow dataset. I also compare surface heat flow near Parkfield and in the well-studied and hydrogeologically simple western Mojave Desert to investigate relationships governing fluid and heat transport in complex geologic terrains.

I find that the characteristics of the heat flow scatter near Parkfield can be generated if the Tertiary sediments that comprise the upper 2-3 km of the crust are characterized by permeability ranging from 3×10^{-16} m^2 to 10^{-15} m^2, allowing recharge of ~ 0.5 cm/yr or higher. Simulated surface heat flow is not sensitive to basement permeability, over a range of realistic depth-dependent permeability functions. Additionally, enhanced permeability resulting from a San Andreas Fault zone and permeability anisotropy in the Tertiary sediments both have a minimal impact on simulated surface heat flow. Although topographically driven groundwater flow through a heterogeneous permeability crust can generate the characteristics of the heat flow scatter near Parkfield, low recharge rates estimated for four springs in the Coast Ranges suggest that the permeabilities and groundwater fluxes required to cause significant advection may not be prevalent on a regional scale. In contrast, the lack of a significant topographic driving force in the western Mojave Desert results in nearly constant heat flow even with sediment permeability as high as 10^{-13} m^2, which is consistent with the low degree of heat flow scatter observed in that area. Lastly, although not the focus of this study, I demonstrate that for a wide range of reasonable permeability architectures in

the upper crust, topographically-driven groundwater flow would not mask a thermal anomaly associated with frictional heating on the San Andreas Fault and also generate the observed scatter in heat flow.

TABLE OF CONTENTS

LIST OF TABLES

LIST OF FIGURES

LIST OF ABBREVIATIONS

bls	below land surface
k	permeability
k_o	permeability at atmospheric pressure
k_v	permeability in the vertical direction
LA	Los Angeles
P_{eff}	Effective Pressure
P_o	Atmospheric Pressure
SAF	San Andreas Fault
SAFOD	San Andreas Fault Observatory at Depth
SF	San Francisco
SUTRA	Saturated-Unsaturated Transport; finite-element modeling code
USGS	United States Geological Survey
y	sensitivity coefficient
z	depth

ACKNOWLEDGMENTS

First, I thank my advisor, Demian Saffer, for guiding me through this project. His honesty, unparalleled attention to detail, and obvious dedication to his students has allowed me to improve tremendously as a student and budding scientist these past two years. I consider myself very lucky to have had Demian as an advisor.

I thank my committee, Kamini Singha and Richard Parizek, as well as my fellow students in the hydro-tectonics group, for their countless useful suggestions and discussions that broadened my knowledge of hydrogeology.

I thank Patrick Fulton for helping me get off to a good start during the early phases of this project, and his enthusiasm and genuine willingness in doing so.

I thank my family and friends for their support through the years. In particular, I am eternally grateful to my parents, Heidi and Anthony Popek, for their constant love and support through all aspects of my academic career and life, and for the numerous road trips "through the wilderness."

Finally, I thank the system administrators in the geology department, Damian Futrick and Tom Canich, for aiding me during my numerous computer crises and hard drive failures that occurred during the course of this modeling project, and for doing so with a sense of optimism.

1. Introduction

1.1 Background

The magnitude and variations of surface heat flow provide insight into a wide range of geologic processes, including faulting and associated seismicity [e.g., *Lachenbruch and Sass*, 1980; *Sibson*, 1982; *Liu and Zoback*, 1997; *Williams et al.*, 2004; *D'Alessio et al.*, 2006], volcanism [e.g., *Blackwell et al.*, 1982; *Henry and Pollack*, 1988], continental rifting and collision [e.g., *Nissen et al.*, 1995], radioactive decay [e.g., *Jaupart et al.*, 1981], groundwater flow [e.g., *Smith and Chapman*, 1983; *Smith and Chapman*, 1985; *Smith et al.*, 1989], climate change [e.g., *Dahl-Jensen et al.*, 1998; *Kooi*, 2008], and sedimentation [e.g. *Jones et al.*, 2003]. Practical applications of surface heat flow observations and temperature surveys in industry and the environmental fields include identifying geothermal, hydrocarbon, and mineral resources [e.g., *Jones et al.*, 2003; *Bouri et al.*, 2007; *Person et al.*, 2008], evaluating groundwater flow systems in contaminant hydrology, managing water resources, [e.g., *Bodvarsson et al.*, 2003; *Becker et al.*, 2004; *Lubis et al.*, 2008], and detecting springs and fractures [e.g., *Silliman and Robinson*, 1989; *Parizek and Parizek*, 2005]. However, because surface heat flow can be influenced by multiple regional and local geologic processes, using heat flow to quantify any one process or property without understanding the other potential influences is problematic [e.g., *Bodvarsson et al.*, 2003; *Galushkin et al.*, 2006; *Kooi*, 2008].

In the California Coast Ranges, spatial variations in regional surface heat flow have been used to study geodynamic processes related to the San Andreas Fault (SAF), particularly its evolution and long-term shear strength [e.g., *Brune et al.*, 1969; *Henyey and Wasserburg*, 1971; *Lachenbruch and Sass*, 1980; *Sass et al.*, 1992; *Goes et al.*, 1997; *Sass et al.*, 1997; *Van Wijk et al.*, 2001; *Guzofski and Furlong*, 2002; *Furlong et al.*, 2003; *Saffer et al.*, 2003; *Fulton et al.*, 2004; *Furlong and Schwartz*, 2004; *Williams et al.*, 2004; *D'Alessio et al.*, 2006; *Erkan and Blackwell*, 2008]. Surface heat flow in the California Coast Ranges exhibits a broad high along strike of the SAF, and is 30-40 mW/m^2 higher than surface heat flow north of Cape Mendocino and 15 mW/m^2 higher than surface heat flow to the south in the Mojave Desert [*Lachenbruch and Sass*, 1980]. The occurrence of relatively low surface heat flow at the Mendocino Triple Junction, and subsequent southward increase and then decrease in surface heat flow in the Coast Ranges to the south along strike of the SAF, is considered to reflect processes related to the northward migration of the triple junction and resulting transition from subduction to transform motion along the west coast of present-day North America [*Goes et al.*, 1997; *Van Wijk et al.*, 2001; *Guzofski and Furlong*, 2002; *Furlong et al.*, 2003; *Furlong and Schwartz*, 2004]. Crustal thickening in advance of the triple junction depresses regional surface heat flow, and crustal thinning and asthenospheric upwelling following its passage increases regional surface heat flow [*Guzofski and Furlong*, 2002].

Quantifying the long-term shear strength of the SAF is a second topic of ongoing research that relies on surface heat flow data in the California Coast Ranges. Assuming hydrostatic pore pressure conditions and ambient shear stress that obeys Byerlee's law for typical rock friction coefficients, the average shear traction on the SAF in the upper 10-15 km (i.e., seismogenic crust) should be in the range 100-200 MPa [e.g., *Byerlee*, 1978; *Brace and Kohlstedt*, 1980; *Scholz*, 2000]. For an average long-term slip rate of 2-4 cm/yr, the SAF should generate a ~ 40 mW/m^2 heat flow anomaly at its trace, decaying to zero by ~ 40 km away from the fault [*Lachenbruch and Sass*, 1980]. This thermal anomaly has not been observed, leading to the interpretation that the SAF slips at shear stress considerably less than predicted by Byerlee's Law [e.g., *Brune et al.*, 1969; *Henyey and Wasserburg*, 1971; *Lachenbruch and Sass*, 1980]. Surface heat flow observations suggest that if a thermal anomaly associated with the SAF does exist, it is no greater than 8-12 mW/m^2 [*Brune et al.*, 1969; *Henyey and Wasserburg*, 1971; *Lachenbruch and Sass*, 1980], corresponding to a resisting shear stress of ~ 20 MPa [*Lachenbruch and Sass*, 1980].

Although trends in observed surface heat flow in the California Coast Ranges both along strike and perpendicular to the SAF have been suggested to reflect fault-related processes, the heat flow data throughout this region exhibit significant scatter that has not been explained. In the well-studied area around Parkfield, CA (Figures 1 and 2a), which is characteristic of the greater Coast Ranges in terms of its subsurface geology and heat flow, surface heat flow ranges from ~ 63 to 94 mW/m^2 [*Lachenbruch and Sass*, 1980; *Sass et al.*, 1997; *Fulton et al.*, 2004] (Table 1) and varies by as much as 20 mW/m^2 over distances of 5-70 km. The standard deviation of the heat flow data near Parkfield is 8.2 mW/m^2. With the exception of a suggested 20 mW/m^2 decrease in

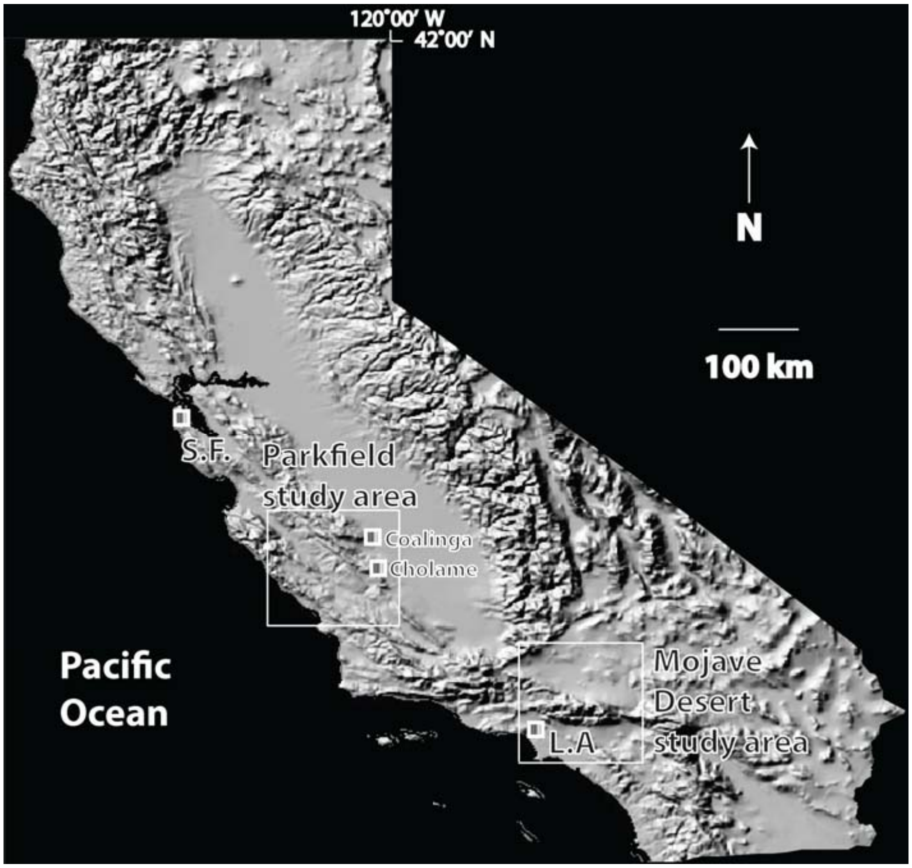

Figure 1

Map of California [*USGS*] showing locations of Parkfield and Mojave Desert study areas. The locations of San Francisco (S.F.), Los Angeles (L.A.), Coalinga, and Cholame are shown for reference.

surface heat flow to the southeast from Coalinga to Cholame that may reflect a long-wavelength regional change in basal heat flux, and which corresponds to a deepening of the base of the seismogenic zone [*Sass et al.*, 1997; *Williams et al.*, 2004], the observed variations in surface heat flow near Parkfield do not exhibit clear trends with lithology or distance from the SAF. In contrast, surface heat flow data elsewhere in the California dataset [*Sass et al.*, 1986; *Sass et al.*, 1994] displays very little variability. In the Mojave area, the standard deviation of the surface heat flow data is 4.8 mW/m^2 [*Sass et al.*, 1986] (Figures 1 and 2b, Table 1), averages 63 mW/m^2 and ranges from 56 mW/m^2 to 74 mW/m^2, but most values are between 62 and 69 mW/m^2.

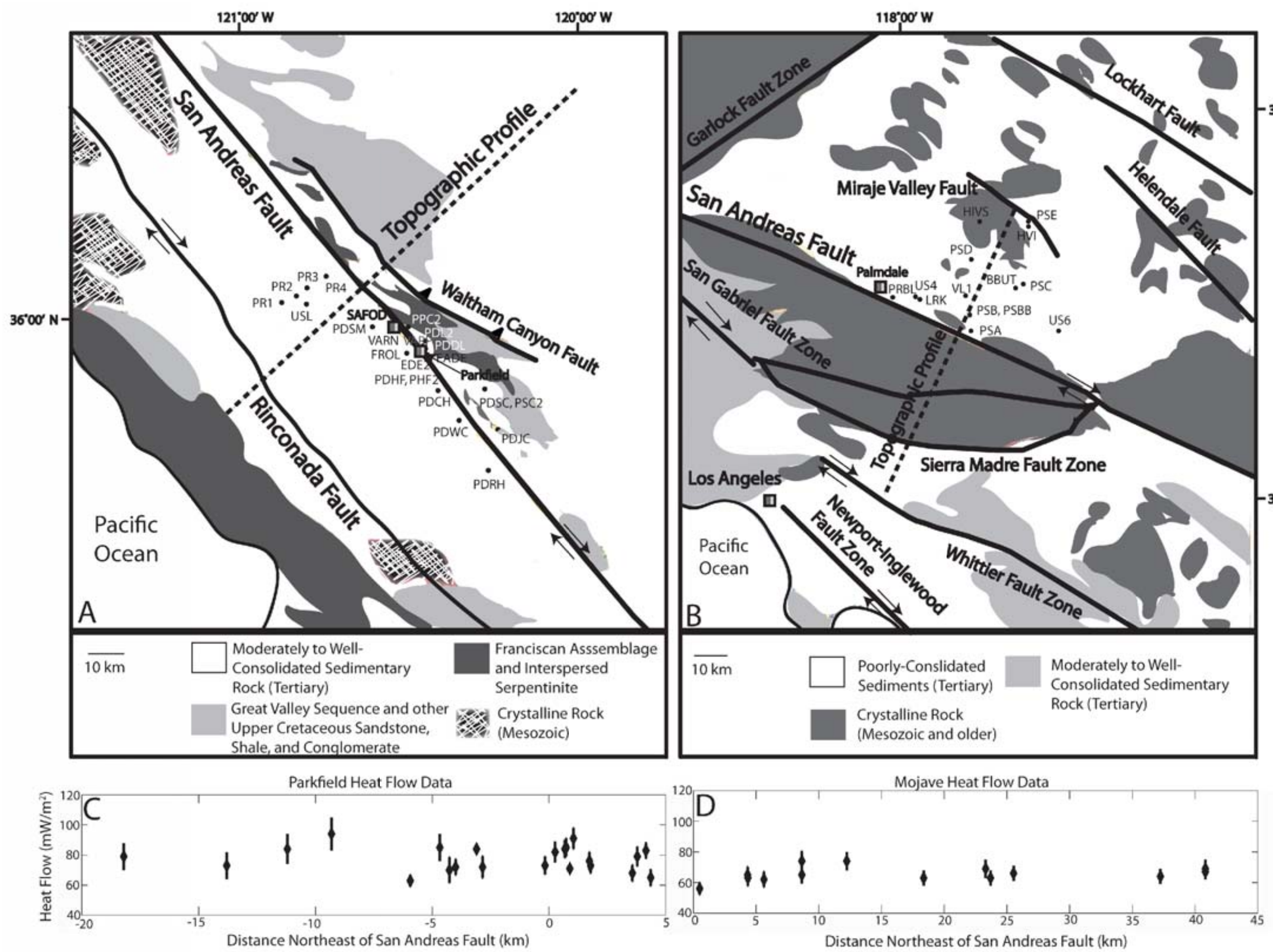

Figure 2
Simplified geologic maps of the (A) Parkfield and (B) Mojave study areas showing the locations of surface heat flow data (C-D, refer to Table 1 for values) and model cross-sections. Maps are modified from Jennings et al., 1977.

Table 1. Observed Surface Heat Flow Near Parkfield, CA and in the Western Mojave Desert Corresponding to Boreholes Displayed in Figure 2

Borehole Name and Abbreviation	Latitude (N)	Longitude (W)	Elevation (m)	Depth Range For Heat Flow (m)	Heat Flow (mW/m^2)
Parkfield [a]					
Cholame Hills (PDCH)	35° 48.7'	120° 24.2'	546	61-182	85 ± 9
Donna Lee, #1 (PDDL)	35° 55.3'	120° 26'	304	61-304	73 ± 5
Donna Lee, #2 (PDL2)	35° 56.2'	120° 25.7'	516	91-207	68 ± 5
Eades Ranch, #1 (EADE)	35° 53.7'	120° 25'	542	152-258	84 ± 6
Eades, #2a (EDE2)	35° 53.6'	120° 25.3'	488	177-277	82 ± 7
Frohlich #1 (FROL)	35° 54.7'	120° 29.1'	547	152-277	72 ± 7
Hefflinger Ranch, #1 (PDHF)	35° 52.7'	120° 23.7'	462	91-305	91 ± 7
Hefflinger Ranch, #2 (PHF2)	35° 52.7'	120° 23.7'	482	122-305	85 ± 6
Jack Canyon #1 (PDJC)	35° 43'	120° 12.3'	469	119-131	83 ± 5
Pancho Rico Canyon, #2 (PR1)	36° 1.9'	120° 51.6'	183	182.9-219.6	79 ± 9
Pancho Rico Canyon, #7 (PR2)	36° 3'	120° 48.7'	226	70.1-128.1	73 ± 9
Pancho Rico Canyon, #12 (PR3)	36° 3.9'	120° 46'	299	60-120	94 ± 11
Pancho Rico Canyon, #19 (PR4)	36° 5.7'	120° 42.5'	555	265-280	84 ± 1
Pine Canyon, #2 (PPC2)	35° 58.2'	120° 28.7'	573	122-203	76 ± 6
Red Hills (PDRH)	35° 37.5'	120° 15.3'	576	183-228	63 ± 3
Stockdale Mt. (PDSM)	35° 58.4'	120° 34.7'	731	80-182	72 ± 5
Stone Corral, #1 (PDSC)	35° 48.6'	120° 16.9'	463	61-122	65 ± 5
Stone Corral, #2 (PSC2)	35° 48.6'	120° 16.9'	451	152-303	79 ± 6
USL 1-3 (USL)	36° 2.9'	120° 46.6'	509	400-475	84 ± 10
Varian Ranch (VARN) deep	35° 57.4'	120° 29.6'	719	63-226	73 ± 6
Varian Ranch, Phillips A-1 (VAR	35° 55.6'	120° 26.8'	509	1219-1555	71 ± 3
White Canyon (PDWC)	35° 44.3'	120° 20.3'	610	187-302	70 ± 8
Western Mojave Desert [b]					
Black Butte (BBUT)	34° 33'	117° 43'	929	122-644	69 ± 6
Chief Paduke (US4)	34° 30.1'	117° 59.5'	954	152-232	65 ± 5
Hi Vista (HVI)	34° 43.9'	117° 41.7'	928	65-107	67 ± 5
Hi Vista, S (HIVS)	34° 44.3'	117° 46.4'	933	130-570	64 ± 5
Little Rock (LTRK)	34° 30.5'	117° 58.7'	936	21-131	62 ± 5
Palmdale Stress A (PSA)	34° 25.6'	117° 51.8'	1302	71-229	63 ± 5
Palmdale Stress B (PSB)	34° 28.1'	117° 51.2'	1076	61-245	65 ± 5
Palmdale Stress B2 (PSBB)	34° 28.1'	117° 51.2'	1076	100-862	74 ± 6
Palmdale Stress C (PSC)	34° 33.2'	117° 42.9'	933	46-213	63 ± 5
Palmdale Stress D (PSD)	34° 39.1'	117° 50.8'	814	115-195	66 ± 5
Palmdale Stress E (PSE)	34° 43.9'	117° 41.7'	928	91-225	69 ± 6
Pear Blossom (PRBL)	34° 31.4'	118° 6.5'	963	122-293	56 ± 4
Phelan (US6)	34° 25'	117° 35'	1306	1067-1768	63 ± 5
Virginia Lee (VL1)	34° 30.3'	117° 50.9'	963	137-259	74 ± 6

[a] Heat flow values and error bars for Parkfield are from *Fulton et al.* [2004]. Heat flow has been corrected for the effects of 3-D topography and variable solar insolation.
[b] Data are from *Sass et al.* [1986].

The scatter in surface heat flow data in the California Coast Ranges has been an obstacle in evaluating geodynamic processes related to the SAF [e.g., *Lachenbruch and Sass*, 1980; *Van Wijk et al.*, 2001; *Saffer et al.*, 2003; *D'Alessio et al.*, 2006], particularly in quantifying frictional heating on the fault [e.g., *Saffer et al.*, 2003]. For example, recent research has focused on the possibility that the SAF may be strong (i.e. slipping at shear stress of 100 MPa averaged over seismogenic depths), but that the heat generated on the fault is redistributed by topographically driven groundwater flow [*Saffer et al.*, 2003; *Fulton et al.*, 2004]. *Saffer et al.* [2003] determined that in the western Mojave Desert, for a wide range of possible crustal and fault permeability architectures, advection of heat by groundwater flow would not mask a frictionally generated heat flow anomaly, and thus the lack in variability in surface heat flow in that region is most consistent with a weak fault. However, the same study was inconclusive near Parkfield due to the substantial scatter in the heat flow data. *Fulton et al.* [2004] corrected the surface heat flow data near Parkfield for terrain effects and determined that it is possible for groundwater flow to mask a thermal anomaly near Parkfield if the upper crust is characterized by homogeneous permeability that is greater than 5×10^{-16} m^2, but this scenario produces a higher standard deviation in surface heat flow than observed, and simulated surface heat flow correlates too strongly with elevation to be consistent with the heat flow data [*Saffer et al.*, 2003].

If upper-crustal processes cause significant variations in surface heat flow, these must be carefully evaluated to interpret heat flow data in the context of geodynamic processes [e.g., *Williams et al.*, 2004; *D'Alessio*, 2006]. Here, I test the hypothesis that heat advection by topographically driven groundwater flow through a subsurface characterized by geologically realistic, heterogeneous permeability can produce the magnitude and spatial characteristics of the scatter in surface heat flow data near Parkfield, CA. To accomplish this, I use a numerical model to simulate coupled fluid and heat transport along a transect perpendicular to the SAF near Parkfield that is representative of the regional topography and geology of the Coast Ranges (Figure 2a). For selected models, I also incorporate a line source of heat on the SAF to test a secondary hypothesis that heat advection through a heterogeneous permeability crust can mask a frictionally generated heat flow anomaly at the trace of the fault [e.g. *Fulton et* *al.*, 2004], but this was not the major purpose of this study. Finally, I simulate coupled fluid flow and heat transport along a transect in the western Mojave Desert (Figure 2b), which is characterized by simpler geology, in order to compare the relationships between simulated surface heat flow, topography, and permeability architecture in regions of differing hydrologic and topographic complexity.

1.2 Processes that Influence Surface Heat Flow

Many processes affect surface heat flow, including terrain effects and thermal refraction. Terrain effects include ground surface temperature variations due to microclimatic effects, dependence of solar heating on latitude, and topographic gradient and refraction. These processes all influence subsurface thermal gradients, most significantly at depths smaller than the scale of topographic relief [*Blackwell et al.*, 1980]. *Fulton et al.* [2004] quantified the effects of 3D topography and variable solar insolation on the Parkfield heat flow dataset, and demonstrated that by accounting for these processes, the standard deviation of the original surface heat flow data was reduced by 26%. *Fulton and Saffer* [2009] also investigated the effects of subsurface thermal refraction and showed that this process could account for the scatter in surface heat flow near Parkfield in a purely conductive regime if the thermal conductivity of the Tertiary sediments is ~ 60% of that for the underlying basement. However, contrasts in thermal conductivity in the Coast Ranges are poorly constrained because rocks from the heat flow boreholes are severely undersampled for thermal conductivity [*Mase et al.*, 1982; *Williams et al.*, 1994; *Sass et al.*, 1997; *Fulton et al.*, 2004].

A third process that can influence surface heat flow is topographically driven groundwater flow. In a topographically driven groundwater system, water that is recharged at high elevations flows down a potential gradient to low elevations or local breaks in slope, where it is discharged [e.g., *Freeze and Witherspoon*, 1967] (Figure 3). Groundwater recharge (downward flow) at high elevations cools the subsurface and creates locally low surface heat flow [e.g., *Smith and Chapman*, 1983; *Smith et al.*, 1989; *Saar and Manga*, 2004]. Groundwater discharge at low elevations advects heat energy upward, creating locally high surface heat flow [e.g., *Smith and Chapman*, 1983; *Smith et al.*, 1989]. In addition to water table configuration, permeability architecture resulting from structural and stratigraphic variability also affects the magnitude and direction of groundwater flow, and therefore influences heat transport [e.g., *Freeze and Witherspoon*, 1967; *Smith and Chapman*, 1983]. The permeability threshold at which advective heat transport becomes significant varies depending on basin geometry, water table slope and configuration, permeability anisotropy, depth of active flow, and the spatial relationships between high and low permeability units [e.g. *Smith and Chapman*, 1983, 1985]. Sensitivity analyses involving realistic values for these parameters suggest that this permeability threshold occurs within a narrow range from ~7×10^{-16} to 3×10^{-16} m^2 for highly simplified basins, but can be higher for very shallow basins with a high degree of permeability anisotropy [e.g. *Smith and Chapman*, 1983, 1985].

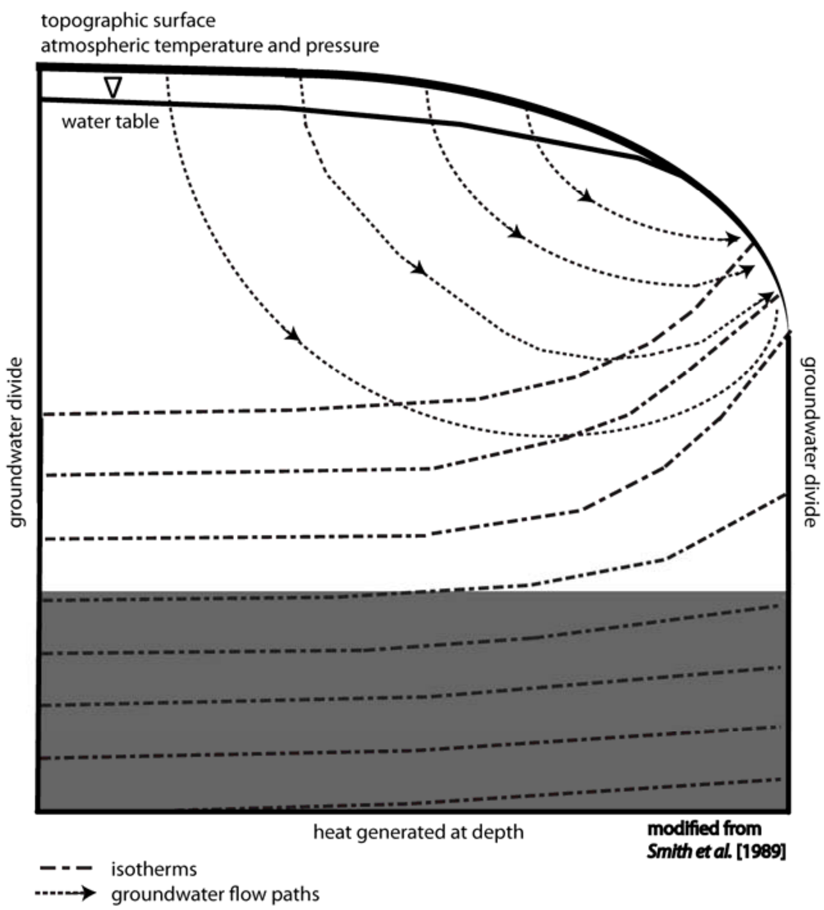

Figure 3

In a topographically driven groundwater system, water at atmospheric temperature and pressure recharges the subsurface at high elevations, resulting in locally low surface heat flow. Water discharges at low elevations, advecting heat upward, resulting in locally high surface heat flow.

Topographically driven groundwater flow has also been recognized as a potential influence on surface heat flow in the California Coast Ranges [e.g., *Williams and Narasimhan*, 1989; *Saffer et al.*, 2003; *Fulton et al.*, 2004]. Although the studies of *Saffer et al.* [2003] and *Fulton et al.* [2004] are broadly consistent with the idea that heat transport near Parkfield is dominated by conduction, the groundwater flow models in these studies employed a highly simplified permeability architecture, which is unrealistic given the known stratigraphic and structural heterogeneity in the California Coast Ranges [e.g., *Dibblee*, 1973; *Jennings et al.*, 1977; *Sims*, 1988, 1990] (e.g., Figure 2a).

2. Geologic and Hydrologic Setting

2.1 Parkfield

The Coast Ranges tectonic province of California is a series of topographic ridges 120-300 km long, 10-50 km wide, and 400-1200 m high, possibly associated with uplift on range-front faults that initiated as early as the late Miocene [*Page et al.*, 1998; *Ducea et al.*, 2003]. The subsurface geology around Parkfield, CA has been well defined by numerous geophysical studies conducted in preparation for (and concurrent with) drilling the San Andreas Fault Observatory at Depth (SAFOD) boreholes ~ 1.8 km SW of the SAF [e.g., *Unsworth et al.*, 1997; *Boness and Zoback*, 2004, 2006; *McPhee et al.*, 2004; *Thurber et al.*, 2004; *Unsworth and Bedrosian*, 2004; *Hole et al.*, 2006; *Becken et al.*, 2008] (Figure 2a), and is broadly representative of the subsurface geology of the greater Coast Ranges [e.g., *Dickinson*, 1966; *Dibblee*, 1973; *Jennings et al.*, 1977; *Sims*, 1988, 1990; *Page et al.*, 1998].

The subsurface geology at Parkfield is characterized by 1-3 km of moderately to well-consolidated Tertiary sediments overlying plutonic, metamorphic and sedimentary basement rock [e.g., *Jennings et al.*, 1977; *Sims*, 1988, 1990; *Bartow*, 1990; *Griscom and Jachens*, 1990; *McPhee et al.*, 2004; *Hole et al.*, 2006] (Figures 2a, 4a). The northwest-southeast striking SAF juxtaposes the allochthonous granitic Salinian block to the southwest and the Franciscan Assemblage to the northeast [e.g., *Dickinson*, 1966; *Jennings et al.*, 1977; *Page et al.*, 1979]. The Franciscan Assemblage is a tectonic mélange [e.g. *Dickinson*, 1966] representing an accretionary prism associated with Mesozoic subduction off the west coast of present-day North America [e.g., *Dickinson*, 1966; *Page et al.*, 1979]. The Waltham Canyon Fault, and other faults associated with the Coast Range Thrust, marks the boundary between the Franciscan Assemblage and the Great Valley Sequence to the northeast [e.g., *Jennings et al.*, 1977; *Jayko et al.*, 1987]. The Great Valley Sequence is a thick package of marine clastics sourced from the Sierran-Klamath belt and deposited in a Mesozoic forearc basin [e.g., *Dickinson*, 1966; *Dickinson and Rich*, 1972; *McLean*, 1981].

The complex geologic structure near Parkfield partly results from subsequent movement on numerous faults in the SAF system [e.g., *Powell et al.*, 1993]. For example, the Jack Ranch, Gold Hill, and Table Mountain Thrusts northeast of the SAF appear to form boundaries between the surface contacts of various sedimentary units [*Sims*, 1988, 1990]. Additionally, siltstones and mudstones containing fossils indicative of the Great Valley Sequence were encountered at the bottom of the main SAFOD borehole immediately southwest of the Franciscan Assemblage [*Bradbury et al.*, 2007, 2008]. This suggests that slivers of the Great Valley Sequence may have been emplaced adjacent to the SAF by strike-slip motion [*Bradbury et al.*, 2007, 2008]. Analyses of core, cuttings, and geophysical data from the SAFOD boreholes indicate that the SAF itself is a highly complex fault zone characterized by numerous compositional and structural elements [e.g., *Bradbury et al.*, 2007; *Evans et al.*, 2007; *Bradbury et al.*, 2008; *Chester et al.*, 2008; *Solum et al.*, 2008]. At least five fault zones with corresponding damage zones and fault cores comprised of gouge and cataclasite were encountered in the boreholes, encompassing both active and inactive strands of the SAF [e.g., *Boness and Zoback*, 2004, 2006; *Bradbury et al.*, 2007; *Evans et al.*, 2007].

Most existing hydrologic data for the California Coast Ranges focus on the coastal aquifers that support large populations [e.g., *Muir*, 1972; *Johnson*, 1980] and not the sparsely populated interior Coast Ranges. However, limited hydrologic data are available for the Parkfield area from monitoring of fault-related deformation and the hydrologic effects of large earthquakes [e.g., *Roeloffs and Quilty*, 1997; *Roeloffs*, 1998; *Roeloffs*, 2001]. Depth to water in five wells in the vicinity of Parkfield ranges from 10 to 25 m below land surface [*Roeloffs and Quilty*, 1997; *Roeloffs*, 1998]. Mean annual precipitation at Parkfield is ~ 40 cm/yr [*Roeloffs*, 2001; *Western Regional Climate Center*, unpublished], but is highly variable from year to year, ranging from 25 to 82 cm/yr from 1987 to 2001 [*Roeloffs*, 2001]. Mean annual temperature near Parkfield ranges from ~ 60 to 90 degrees Fahrenheit [*Western Regional Climate Center*, unpublished].

2.2 Western Mojave Desert

The western Mojave Desert southeast of the Coast Ranges is bounded by the SAF to the southwest and by the Garlock Fault to the north [*Jennings et al.*, 1977] (Figure 2b). Topographic relief is related to the San Gabriel Mountains to the southwest of the SAF, and to various basement uplifts northeast of the SAF separating otherwise low-gradient sedimentary basins that trend roughly parallel to the trace of the SAF [*Jennings et al.*, 1977]. Geophysical studies suggest that the regional geologic architecture of the western Mojave Desert adjacent to the San Gabriel Mountains is relatively simple, consisting of ~ 500 m to over 1500 m of Tertiary and Quaternary sediments overlying crystalline bedrock [e.g., *Pellerin and Christensen*, 1998; *Lutter et al.*, 1999; *Fuis et al.*, 2001a, 2001b]. Crystalline basement of the San Gabriel Mountains and exposed basement northeast of the SAF consists of a variety of plutonic and metamorphic rocks bounded by major regional active faults that dip to the northeast [*Jennings et al.*, 1977; *Fuis et al.*, 2001a, 2001b].

Limited hydrologic data in the western Mojave Desert also suggest a shallow water table. The pre-development potentiometric surface in the western Mojave Desert in 1915 was at or above the ground surface in many areas, but today groundwater levels are ~ 30 to 100 m deeper [e.g., *Durbin*, 1978; *Sneed and Galloway*, 2000]. Mean annual rainfall in the western Mojave Desert ranges from 12-20 cm [*Western Regional Climate Center*, unpublished], but can vary from more than 100 cm near the crest of the San Gabriel Mountains to less than 8 cm in the valley floors [*Rantz*, 1969]. Mean annual temperature ranges from 60 to 95 degrees Fahrenheit [*Western Regional Climate Center*, unpublished].

3. **Methods**

3.1 Model Domains and Boundary Conditions

I simulate 2D steady-state coupled fluid and heat transport using the finite element code SUTRA [*Voss*, 1984]. For Parkfield, my model domain extends for 116 km, from the Coast Ranges northeastward to the Great Valley along the profile displayed in Figure 2a, perpendicular to the SAF and to regional topographic trends (Figure 4a). For the Mojave, my model domain extends for 99.8 km from the San Gabriel Valley northeastwards to the Miraje Valley Fault along the profile displayed in Figure 2b (Figure 4b). I obtained these topographic profiles from Digital Elevation Models of California and interpolated elevations to 100 m horizontal spacing.

The endpoints of each topographic profile coincide with assumed regional groundwater divides, and therefore I set the lateral boundaries in both models as no-flow boundaries for fluid and heat. The basal boundary of each model is 10 km below sea level, and I assign it as a no-flow boundary for fluid. I also assign a heat flux of 78 mW/m^2 and 63 mW/m^2 to the basal boundary in the Parkfield and Mojave models, respectively, corresponding to the average surface heat flow in each region [*Lachenbruch and Sass*, 1980]. Based on well data that indicate the water table is shallow near Parkfield and in the western Mojave Desert [*Durbin*, 1978; *Roeloffs and Quilty*, 1997; *Sneed and Galloway*, 2000; *Roeloffs*, 2001], I assume that the potentiometric surface is the topographic surface; this provides a maximum driving force for groundwater flow and thus the largest possible advective perturbation to simulated heat flow for a given model geometry and permeability architecture. I assign a constant atmospheric pressure of 0.1 MPa and a temperature lapse rate of 6.9 °C per km at the top boundary in each model, with a temperature of 10 °C at sea level. In a subset of simulations for the Parkfield model, I also include a line source of heat on the SAF. The heat source increases linearly by 8.85 mW/m^2 per km depth, corresponding to an average slip rate on the SAF of 3.1 cm/yr and an average resisting shear stress of 9 MPa/km over the seismogenic zone [*Lachenbruch and Sass*, 1980].

I test the numerical stability of the finite element grid for both the Parkfield and Mojave models by reducing the grid size until simulated surface heat flow no longer changes and the total thermal energy input at the base of each model equals the thermal energy output at the topographic surface. For the Parkfield model, I use an element size of 150 m for the upper 6 km of the subsurface and 200 m for the lower 5 km. I use an element size of 200 m for the Mojave model except for the highest permeability simulation, in which I use an element size of 50 m in the Tertiary sediments in order to adequately model the high spatial gradients in pressure and temperature accompanying increased flow rates. I also test the response of both models to smoother topography by interpolating elevations with a horizontal spacing of 1500 m. Simulated surface heat flow is not sensitive to a further decrease in element size or to smoother topography in either model.

I extract simulated heat flow from 150-300 m depth below land surface (bls) to be consistent with the depth ranges represented in the heat flow dataset (Table 1). In the Parkfield study area, the surface heat flow data were obtained exclusively from boreholes drilled southwest of the Waltham Canyon Fault (Figure 2a). In the Mojave Desert study area, heat flow data were obtained from boreholes drilled exclusively in the sediments and crystalline basement northeast of and at the trace of the SAF (Figure 2b). To ensure that the simulated surface heat flow that I analyze is associated with similar regional topographic and lithologic characteristics as the data, I include only the simulated surface heat flow from positions 0-64 km along the topographic profile in the Parkfield model (the Coast Ranges) and 61-99.8 km along the topographic profile in the Mojave model (the western Mojave Desert) when comparing the model output with the heat flow data (Figure 4).

3.2 <u>Permeability and Porosity Architecture</u>

I use previously published geologic maps, well data, and interpretations of subsurface geology from geophysical studies to define composite geologic cross-sections for the Parkfield and Mojave regions that encompass the key hydrogeologic units [*Mabey*, 1960; *Jennings et al.*, 1977; *Mansfield*, 1979; *Page et al.*, 1979; *Sims*, 1988, 1990; *Bartow*, 1990; *Griscom and Jachens*, 1990; *Londquist et al.*, 1993; *Lutter et al.*, 1995; Pellerin and Christensen, 1998; *Lutter et al.*, 1999; *Sneed and Galloway*; 2000; *Boness and Zoback*, 2004, 2006; *McPhee et al.*, 2004; *Hole et al.*, 2006; *Guzofski et al.*, 2007; *Becken et al.*, 2008; *Fuis et al.* 2001a, 2001b] (Figure 4). The key hydrogeologic

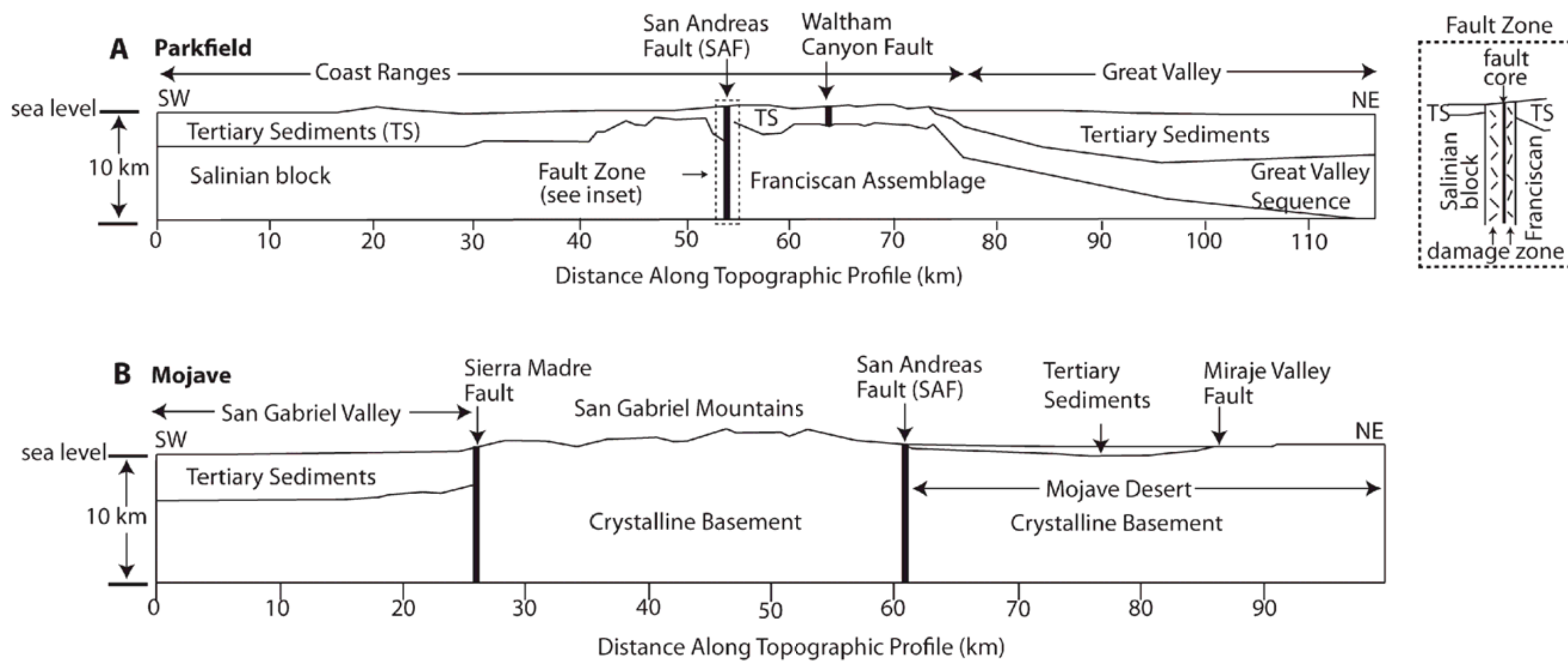

Figure 4
Model cross-sections of the (A) Parkfield and (B) Mojave Desert study areas. Sections are based on geologic and geophysical interpretations describing the positions and geometries of the major lithologic units in each study area (refer to descriptions in text). The locations of the cross-sections are shown in Figure 2. Inset shows components of the fault zone architecture included in a subset of simulations for the Parkfield area.

units in the Parkfield study area are the Tertiary sediments, Cretaceous Salinian block, Jurassic-Cretaceous Franciscan Assemblage, Jurassic-Cretaceous Great Valley Sequence, and San Andreas Fault zone. I refer to the Salinian block, Franciscan Assemblage, and Great Valley Sequence collectively as "basement". The key hydrogeologic units in the Mojave study area are the Tertiary sediments and crystalline basement. The Tertiary sediments in both study areas consist of several formations.

For each major rock unit, I constrain permeability (*k*) and porosity using previously published values obtained from laboratory and in-situ measurements (Table 2), and systematically vary permeability to investigate the sensitivity of simulated surface heat flow to the permeability assigned to each unit (Table 2). I assign a grain thermal conductivity of 2.9 W/m K for all units in both models to exclude the effects of thermal refraction from simulated surface heat flow, which have already been explored in detail [*Fulton and Saffer*, 2009]. In the following sections, I provide a more detailed description of the thickness, geometry, permeability, and porosity of each hydrogeologic unit.

3.2.1. <u>Tertiary Sediments</u>

In the Parkfield area, Tertiary sediments directly overlie metamorphic and plutonic rocks of the Salinian block west of the SAF, and overlie Franciscan Assemblage and Great Valley Sequence northeast of the SAF (Figure 4a). Lithologies range from near-shore gravel and sandstone to deep-marine mudstone (Table 2), and are locally interspersed with marble, biotite, and tonalite [*Sims*, 1988, 1990]. The Paso Robles, Santa Margarita, and Pancho Rico Formations are present exclusively to the southwest of the SAF. To the northeast of the SAF, the Etchegoin, Monterey, and Temblor are the dominant formations in the Coast Ranges [*Sims*, 1988, 1990]. The Varian Ranch Formation is present locally in the Parkfield Syncline. The Tertiary sediments in the Great Valley include the Tulare, San Joaquin, Etchegoin, Santa Margarita, Reef Ridge, Monterey, Temblor, Kreyenhagen, Lodo, and Moreno Formations [e.g., *Mansfield*, 1979; *Bartow*, 1990; *Guzofski et al.*, 2007]. Although the Tertiary sediments in the Parkfield area are comprised of multiple discrete units of varying thickness, I treat the sediments in my model as a single hydrologic unit.

The total thickness of the Tertiary sediments varies in the Parkfield area. They are over 1500 m thick in the Parkfield Syncline [*Sims*, 1990], but thin southeastward towards Cholame where basement outcrops are exposed at the surface [*Sims*, 1988, 1990]. The sediments are 768 m thick in the SAFOD pilot hole 1.8 km SW of the SAF [*Boness and Zoback*, 2004] and 780 m thick in the main hole immediately adjacent to the pilot hole [*Boness and Zoback*, 2006]. I use the sediment-basement contact imaged in geophysical studies along transects perpendicular to the SAF near Parkfield, and described in well data, to define sediment thickness in my model [*Bartow*, 1990; *Griscom and Jachens*, 1990; *McPhee et al.*, 2004; *Hole et al.*, 2006] (Figure 4a). The base of the Tertiary sediments is constrained by seismic refraction data to be at 2 km depth 20 km southwest of the SAF [*Hole et al.*, 2006]. Sediment thickness further southwest along profile is not as well-constrained, so I allow the thickness of the sediments to increase linearly to 2.5 km at the southwestern limit of my model domain based on regional geological and geophysical studies [*Page et al.*, 1979]. Thickness in the section between 20 km southwest and 10 km northeast of the SAF ranges from 0.5 to 2 km, and is well-defined by seismic and gravity transects that include the SAFOD boreholes [*McPhee et al.*, 2004; *Hole et al.*, 2006]. I use well data to constrain the thickness of the Tertiary sediments in the Great Valley, which reaches a maximum of > 4.5 km [*Bartow*, 1990].

I define the equivalent vertical permeability for the Tertiary sediments as 10^{-15} m^2, based on the reported permeabilities of individual formations (Table 2) and assuming equal thicknesses and horizontal layering for the stratigraphic assemblages in the study area [*Sims*, 1988, 1990]. Many of the previously published formation permeabilities were measured in the laboratory on cores from productive oil fields in the San Joaquin Valley, and therefore create a geographic and sampling bias in estimating regional sediment permeability. To investigate the sensitivity of simulated surface heat flow to the permeability of the Tertiary sediments, I consider a range of permeability for the package from 10^{-15} to 10^{-20} m^2, assuming isotropic permeability (Table 2). I also consider the possibility of permeability anisotropy created by sedimentary layering by investigating vertical permeability ranging from 10^{-15} to 10^{-17} m^2, and assigning anisotropy ratios (horizontal permeability relative to vertical permeability) up to 10 (Table 2). Based on the range of data available, I assign a porosity of 35% for the

Table 2. Permeability and Porosity of Hydrologic Units in the Parkfield Area

Unit / Formation	Permeability (m^2)	Porosity	References [a]
1. Tertiary Sediments sandstones, mudstones, and conglomerates; some gravel, silt, sand	**OBSERVED**: $k = 4\times10^{-13}$ (Santa Margarita), up to 8×10^{-12} (Etchegoin), average 6×10^{-16} (Monterey), 2×10^{-14} to 4×10^{-12} (Temblor) **MODELED**: $k = 10^{-15}$ to 10^{-20} (isotropic) anisotropic: $k_h = 10^{-14} - 10^{-16}$, $k_v = 10^{-15} - 10^{-17}$	**OBSERVED**: 30-35% **MODELED**: 35%	1-11
2. Salinian Granite fractured granite with localized shear zones	**OBSERVED**: $k = \sim 10^{-15} - 10^{-18}$ $0 \le z \le 2$ km bls; k decreases by ~ 1 order of magnitude per km depth **MODELED**: Low: $k = 10^{-20}$ High: $\begin{cases} k = 10^{-15} & z \le 1 \text{ km bls;} \\ k = 10^{-15 - [z - 1]} & 1 \le z \le 6 \text{ km bls;} \\ k = 10^{-20} & z \ge 6 \text{ km bls} \end{cases}$	**OBSERVED**: 1-2% (matrix) **MODELED**: 5%	12-17
3. Franciscan Assemblage greenstone, greywacke, chert, and blueschist in a matrix of cataclasite	**OBSERVED**: not available **MODELED**: Low: $k = 10^{-20}$ High: $k = -3.2 \times \log[z\,(\text{km})] - 14$; $k \le 10^{-14}$ [b]	**OBSERVED**: max 6.2% typically < 2% **MODELED**: 5%	18-19
4. Great Valley Sequence sandstones, mudstones, and conglomerate lenses	**OBSERVED**: $k \le 10^{-15}$ from surface exposures **MODELED**: Low: $k = 10^{-20}$ High: $k = 10^{-15}$	**OBSERVED**: average 10% **MODELED**: 10%	20-24
5. San Andreas Fault Damage Zone highly fractured rock	**OBSERVED**: not available **MODELED**: 10x: $k = (k_{\text{country rock}}) \times 10$ 100x: $k = (k_{\text{country rock}}) \times 100$; $k \le 10^{-14}$ [b]	**OBSERVED**: 2-15% **MODELED**: 10%	16-17, 25-27
6. San Andreas Fault Core gouge and cataclasite	**OBSERVED**: $k = 10^{-20}$ **MODELED**: $k = 10^{-20}$	**OBSERVED**: not available **MODELED**: 10%	28

[a] References are 1. *Wylie et al.* [1996], 2. *Coburn and Gillespie* [2002], 3. *Link et al.* [1986], 4. *Harmsen and Merrill* [1988], 5. *Dholakia et al.* [1998], 6. *Montgomery and Morea* [2001], 7. *Clark et al.* [2001], 8. *Bridges and Castle* [2001], 9. *Galehouse* [1967], 10. *Sims* [1990], 11. *Whittlesey and Bottjer* [1998], 12. *Zoback* [1982], 13. *Coyle and Zoback* [1988], 14. *Morrow and Byerlee* [1988], 15. *Morrow and Byerlee* [1992], 16. *Boness and Zoback* [2004], 17. *Boness and Zoback* [2006], 18. *Stewart and Peselnick* [1977], 19. *Manning and Ingebritsen* [1999], 20. *Dibblee* [1973], 21. *Dickinson and Rich* [1972], 22. *McLean* [1981], 23. *Unsworth and Bedrosian* [2004], 24. *Yang and Aplin* [2007], 25. *Ikari et al.* [2009], 26. *Crawford et al.* [2008], 27. *Faulkner* [2004], and 28. *Morrow, Shi, and Byerlee* [1981]

[b] Regardless of z or $k_{\text{country rock}}$, permeability greater than 10^{-14} m^2 was not included in the model

Tertiary sediments (Table 2).

The late Tertiary-Quaternary sediments and sedimentary rock in the Mojave Desert consist of poorly sorted conglomerate, sandstone, siltstone, shale, limestone, and dolomite [*Londquist et al.*, 1993; *Sneed and Galloway*, 2000]. A regional confining unit separates aquifers in the sedimentary sequence in some areas, but I do not incorporate this confining unit in my model because its nature and geometry are not known. Well tests indicate that the permeability of the sediments may be as high as 10^{-13} m^2 [*Durbin*, 1978; *Sneed and Galloway*, 2000]. In the Mojave simulations, I assign the crystalline basement a permeability of 10^{-20} m^2 and consider a range of isotropic permeability for the Tertiary sediments ranging from 10^{-20} to 10^{-13} m^2.

I constrain the thickness of the sediments in my Mojave model based on seismic refraction and reflection data from the LARSE I (Los Angeles Regional Seismic Experiment) line, which is nearly coincident with my model transect, and supplemented by sparse well data [*Brocher et al.*, 1998]. These datasets suggest that the Tertiary sediments are 3.7 km thick 15 km SW of the Sierra Madre Fault, remain at least this thick in the San Gabriel Valley, and thin abruptly at the contact with the Sierra Madre Fault to the northeast [*Lutter et al.*, 1999] (Figure 4b). Crystalline rock of the San Gabriel Mountains outcrops from the Sierra Madre Fault northeastwards to the SAF [*Jennings et al.*, 1977]. Sediment thickness northeast of the SAF (in the western Mojave Desert) is variable among the sedimentary basins. Bouguer gravity anomalies suggest that the sediments in the vicinity of the profile are not as thick as in the neighboring Lancaster basin [*Mabey*, 1958], where they may be locally over 1500 m thick [*Londquist et al.*, 1993; *Sneed and Galloway*, 2000]. On the basis of results from the LARSE experiment [*Lutter et al.*, 1995, *Pellerin and Christensen*, 1998], I define the sediment-basement contact immediately northeast of the SAF at 500 m below the land surface, deepening to 800 m below land surface 15 km northeast of the SAF, and shallowing to 0 m 25 km northeast of the fault, where basement rocks are exposed at the surface [*Jennings et al.*, 1977] (Figure 4b).

3.2.2 Granitic and Metamorphic Basement

The granitic Salinian block underlies the Tertiary sediments to the southwest of the SAF (Figure 4a). Although permeability measurements for the Salinian block in the Parkfield area are not readily available, permeability measurements on granitic rock in the Mojave Desert south of the terminus of the Salinian terrane provide some relevant constraints, based on geographic proximity and a similar history of mineralization resulting from fluid flow [*Morrow and Byerlee*, 1988, 1992; *Bradbury et al.*, 2007]. Laboratory permeability measurements for crystalline rock samples obtained from the Cajon Pass scientific borehole (primarily granodiorite) in the Mojave region decrease from a value of 10^{-18} m^2 at an effective stress equivalent to a depth of 500 m, by approximately one order of magnitude per km burial depth [*Morrow and Byerlee*, 1988, 1992] (Table 2). Although these permeabilities were measured in the laboratory on intact core samples, the in-situ permeability at Cajon Pass was measured using slug tests as 1.67×10^{-18} m^2 between 1829 and 2115 m depth [*Coyle and Zoback*, 1988], and is consistent with the laboratory results. Isotopic studies also suggest poor fracture connection and therefore low permeability in these basement rocks [e.g., *Hammond et al.*, 1988; *Kharaka et al.*, 1988]. However, in-situ permeability of the plutonic rocks measured using slug tests at the XTLR well northeast of the SAF in Palmdale, CA for various intervals between 99-869 m depth is ~ 10^{-15} m^2 [*Zoback*, 1982], suggesting that shallow sections of the granitic basement may have locally high permeability, probably related to fractures [e.g., *Brace*, 1980].

Based on the permeability observations described above, I consider two cases for the permeability of the Salinian block in my model. In the first case, I assign this unit a homogeneous permeability of 10^{-20} m^2, herein termed "Low" permeability (Table 2). However, it is also possible that at shallow depths, the permeability of the Salinian block may be high enough to permit significant groundwater flow. Therefore, I define a second case for the permeability of this unit, termed "High" permeability, which incorporates the observations discussed above and likely provides an upper bound for its permeability (Table 2, Figure 5):

$$k = 10^{-15}\,\mathrm{m}^2 \qquad \text{for } z < 1 \text{ km bls} \qquad (1)$$

$$k = 10^{(-15-[z-1])}\,\mathrm{m}^2 \qquad \text{for } 1 \le z \le 6 \text{ km bls} \qquad (2)$$

$$k = 10^{-20}\,\mathrm{m}^2 \qquad \text{for } z \ge 6 \text{ km bls} \qquad (3)$$

Observations from the SAFOD boreholes suggest that the matrix porosity of the Salinian block is 1-2% [*Boness and Zoback*, 2006], comparable with the suggested low porosity associated with extensive crack healing, sealing, and recrystallization in granitic samples from Cajon Pass [*Morrow and Byerlee*, 1992]. I assume a porosity of 5% for the Salinian block in the Parkfield model (Table 2) to account for fracturing that likely increases the porosity of this unit beyond the reported value for the matrix as measured at the core scale [e.g., *Davis*, 1969].

3.2.3 Franciscan Assemblage

The Jurassic - Cretaceous Franciscan Assemblage underlies the Tertiary sediments to the northeast of the SAF (Figure 4a), and underthrusts the Great Valley Sequence along faults associated with the Coast Range Thrust [*Jayko et al.*, 1987]. It also outcrops in several locations between the San Andreas and Waltham Canyon Faults in the study area (Figure 2a). The Franciscan is a mélange, and is dominantly a sheared metagraywacke with variably-sized clasts of greenstone, greywacke, chert, and blueschist [*Dibblee*, 1973]. Due to its variable lithology, the regional permeability of the Franciscan Assemblage is difficult to estimate.

I consider two cases to define the permeability of the Franciscan Assemblage. First, I use a permeability-depth relationship derived by *Manning and Ingebritsen* [1999] specifically for crustal rocks undergoing prograde metamorphism (equation 4), termed "High" permeability (Table 2). This is consistent with the abundance of carbon dioxide in springs associated almost exclusively with the Franciscan Assemblage, along with modeling studies, which suggest that it is undergoing prograde metamorphic dehydration driven by crustal temperature changes associated with the migration of the Mendocino Triple Junction [*Irwin and Barnes*, 1975; *Lachenbruch and Sass*, 1980; *Johnson and O'Neil*, 1984; *Kennedy et al.*, 1997; *Guzofski and Furlong*, 2002; *Furlong et al.*, 2003].

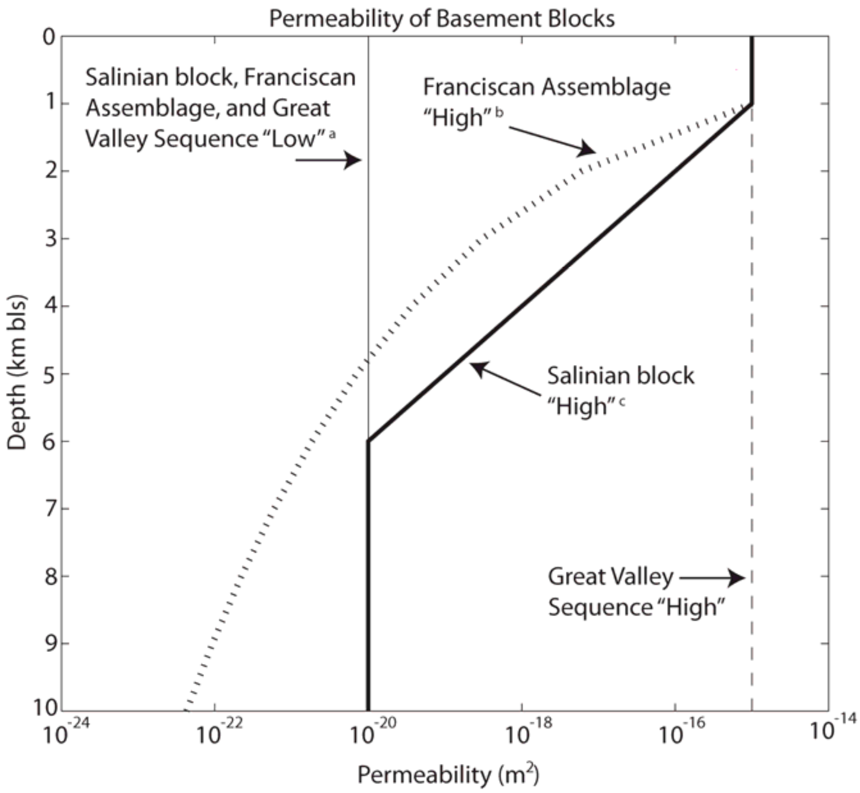

Figure 5

Permeability used in Parkfield model for basement units, including the Salinian block, Great Valley Sequence, and Franciscan Assemblage, as described in text, as a function of depth. Sources are (a) *Morrow and Byerlee* [1988, 1992], *Yang and Apling* [2007], (b) *Manning and Ingebritsen* [1999], and (c) *Morrow and Byerlee* [1988, 1992], *Zoback* [1982], and *Coyle and Zoback* [1988].

Second, I assign the Franciscan a homogeneous permeability of 10^{-20} m^2, termed "Low" permeability (Table 2), in order to isolate the effects of advective heat transport only in the overlying sediments. I set maximum permeability as 10^{-14} m^2 in my model, regardless of depth.

$$k = -3.2 \times \log[z(km) - 1] - 14\,;\; k \leq 10^{-14}\ \mathrm{m}^2 \tag{4}$$

I assign a porosity of 5% for the Franciscan Assemblage, based on laboratory measurements for a variety of rock types and metamorphic grades in the Franciscan Assemblage that yield a maximum porosity of 6.2% (Table 2), with most values less than 2% [*Stewart and Peselnick*, 1977].

3.2.4 Great Valley Sequence

The Great Valley Sequence overthrusts the Franciscan Assemblage to the northeast of the SAF in the Parkfield area, and outcrops on a regional scale in the Great Valley and at numerous locations near the SAF (Figure 2a). The Waltham Canyon Fault is the contact between the Great Valley Sequence and Franciscan Assemblage (Figure 2a), and is ~ 10 km northeast of the SAF in the study area [*Jennings et al.*, 1977]. This contact and the contact 20 km northeast of the SAF between the Great Valley Sequence and Tertiary sediments in the Great Valley (Figure 4a) are representative of the positions of the regional contacts between the Franciscan Assemblage, Tertiary sediments, and Great Valley Sequence northeast of the SAF [e.g., *Jennings et al.*, 1997]. The Great Valley Sequence consists of 15 km of moderately to poorly-sorted, subangular, lithofeldspathic sandstones, silty mudstones, and conglomerate lenses [e.g., *Dickinson and Rich*, 1972; *Dibblee*, 1973] and forms a regional syncline in the Great Valley [*Griscom and Jachens*, 1990; *Becken et al.*, 2008]. I define the base of the Great Valley Sequence in my model based on a combination of gravity, magnetic, and electrical resistivity studies [e.g., *Griscom and Jachens*, 1990, *Becken et al.*, 2008] (Figure 4a).

I consider two cases for the permeability of the Great Valley Sequence. First, I assign this unit a homogeneous permeability of 10^{-15} m^2, termed "High" permeability, based on laboratory-derived permeability measurements for Great Valley Sequence mudstones exposed at the surface west of the Sacramento Valley [*McLean*, 1981] (Table 2). This high-permeability scenario is designed to assess the maximum effects of groundwater flow through the Great Valley Sequence, Franciscan Assemblage and Tertiary sediments on simulated surface heat flow. Second, I consider a scenario termed "Low" permeability based on laboratory tests on mudstones [*Yang and Aplin*, 2007], in which I assign the unit a permeability of 10^{-20} m^2 (Table 2). I assume a porosity of 10% in my model (Table 2), corresponding to the average porosity of sandstone outcrops west of the Sacramento Valley [*McLean*, 1981] and that estimated from magnetotelluric studies [*Unsworth and Bedrosian*, 2004].

3.2.5 Fault Zone

Brittle fault zones are typically characterized by a clay-rich core encompassing the slip surface, and an adjacent damage zone composed of small faults, veins, fractures, and other deformational features formed in response to slip on the main fault [e.g., *Caine et al.*, 1996]. If a core is present, its low permeability may create a barrier to across-fault flow [e.g., *Caine et al.*, 1996]. Geophysical and petrologic observations suggest the presence of a complex damage zone surrounding the SAF [*Boness and Zoback*, 2004, 2006; *Bradbury et al.*, 2007; *Evans et al.*, 2007; *Bradbury et al.*, 2008; *Chester et al.*, 2008; *Solum et al.*, 2008]. Based on contrasting helium isotope ratios and pore pressures across fault zones encountered in the SAFOD boreholes, the SAF has been interpreted to act as a barrier to regional groundwater flow [e.g., *Bradbury et al.*, 2007; *Evans et al.*, 2007; *Solum et al.*, 2007; *Wiersberg and Erzinger*, 2007; *Chester et al.*, 2008]. I investigate a suite of simplified fault zone permeability architectures in a subset of simulations for Parkfield, which include a damage zone with and without a central low-permeability fault core (Figure 4a, inset). I define the southwestern boundary of the damage zone at 1.6 km SW of the SAF, corresponding to the transition into highly fractured, damaged rock (relative to "background" levels of fracturing) encountered in the SAFOD main borehole [*Boness and Zoback*, 2006]. I define the northeastern limit of the damage zone at 1 km NE of the SAF, based on the extent of a zone of low electrical resistivity and seismic attenuation interpreted to reflect a saturated zone of increased fluid content [*Unsworth et al.*, 1997; *Bennington et al.*, 2008].

I consider three cases for the permeability architecture of the fault zone (Table 2). In the first two cases, I simulate a fault conduit by assigning the permeability of the damage zone as one and two orders of magnitude greater than the adjacent country rock (Table 2); these simulations are termed "10x" and "100x," respectively. In a third case, I simulate a fault zone that acts as a conduit-barrier by including a 200 m wide central zone with a permeability of 10^{-20} m^2 within the 2.6 km wide damage zone. This permeability is consistent with laboratory measurements of permeability for fault gouge from the SAF at Cienega Valley, and approximates values of permeability for other synthetic and natural gouges [*Morrow, Shi, and Byerlee*, 1981; *Faulkner*, 2004; *Crawford et al.*, 2008;

Ikari et al., 2009]. I assume a porosity of 10%, based on measured porosity in the SAFOD pilot hole from downhole logs [*Boness and Zoback*, 2004] (Table 2).

3.3 Permeability Sensitivity Analysis

For the Parkfield study area, I test the sensitivity of simulated surface heat flow to the permeability of the Tertiary sediments, basement permeability, fault zone architecture, and permeability anisotropy in the Tertiary sediments. First, I test the sensitivity of simulated surface heat flow to the permeability of the Tertiary sediments by investigating a range of permeability (isotropic) for the sediments, while including a low-permeability basement. Second, I test the sensitivity of simulated surface heat flow to basement permeability by considering the "high" and "low" permeability scenarios for each basement unit, using the functions described in Section 3.2 and illustrated in Figure 5. When I assign the "low" permeability functions or the "high" permeability functions to all of the basement blocks, I collectively term these scenarios "low-permeability basement" and "high-permeability basement." I explore the effects of basement permeability for the full suite of sediment permeability and do not include a fault zone in these simulations. Third, I test the sensitivity of simulated surface heat flow to fault zone permeability architecture by considering the fault conduit and conduit-barrier cases described in Section 3.2.5, over the full range of sediment permeability and for a low-permeability basement (Table 2). Fourth, I test the sensitivity of simulated surface heat flow to permeability anisotropy in the Tertiary sediments. I do not incorporate a fault zone in these simulations, and include low-permeability basement.

For the Mojave study area, I investigate the sensitivity of simulated surface heat flow only to the permeability of the sediments, and consider a range of sediment permeability from 10^{-15} to 10^{-13} m^2. For these simulations, I assign the basement a permeability of 10^{-20} m^2. I do not evaluate the sensitivity of simulated surface heat flow to basement permeability, fault zone permeability, or permeability anisotropy in the sediments, because results from simulations testing the effects of isotropic sediment permeability illustrate that topography is much more important than small heterogeneities in subsurface permeability architecture in determining the strength of advective heat transport in this region (assuming a realistic permeability architecture).

3.4 Analysis of Model Output

To define near-surface heat flow from model simulations, I extract temperatures at 150-300 m bls from the simulated steady-state temperature fields. As noted above, this depth range is comparable to that used to determine heat flow in most boreholes for the Parkfield and Mojave data sets [*Lachenbruch and Sass*, 1980; *Sass et al.*, 1986; *Sass et al*, 1994; *Sass et al.*, 1997; *Saffer et al.*, 2003; *Fulton et al.*, 2004] (Table 1). In addition, I remove conductive topographic refraction effects from simulated heat flow in order to compare with the data, which have been corrected for these effects in the Parkfield area [*Fulton et al.*, 2004]. To remove conductive topographic refraction effects from simulated surface heat flow, I run a suite of conduction-only models to determine the magnitude of topographic refraction along the profile, and subtract this result from simulated surface heat flow in all other simulations. For the Mojave heat flow data, I assign error bars of ± 8% to the heat flow data, which corresponds to the average topographic and terrain correction for the Parkfield data [*Fulton et al.*, 2004]. However, error associated with the Mojave dataset is most likely even less than this because of the lack of topographic variability northeast of the San Andreas Fault (Figure 4b).

4. Results

4.1 Parkfield

First, I consider the effects of the permeability of the Tertiary sediments on simulated surface heat flow. Heat advection through a heterogeneous permeability upper crust produces less variability in surface heat flow than the homogeneous permeability case (Figure 6), and decreases the standard deviation of surface heat flow by as much as 19 mW/m^2 for sediment permeability of 10^{-15} m^2 (Figure 7a). This is consistent with previous modeling results [e.g., *Freeze and Witherspoon*, 1967, *Smith and Chapman*, 1983], in that the reduced depth of groundwater circulation in the heterogeneous permeability case decreases the magnitude of advective disturbance (Figures 6-7). Exceptions to this pattern occur at positions 52 km and 62 km along the profile, where simulated surface heat flow at discharge zones is increased compared with the homogeneous permeability case. The standard deviation of simulated surface heat flow ranges from 0.2 to 21.5 mW/m^2 for sediment permeability ranging from 10^{-17} to 10^{-15} m^2

(Table 3, Figure 7a). Simulated mean recharge (expressed as a mass flux per unit area) ranges from 0.02 to 1.69 cm/yr over the same range in sediment permeability (Table 3, Figure 7b). Although variability in simulated surface heat flow is dependent upon both sediment permeability and depth of flow, simulated mean recharge is essentially the same for a given sediment permeability for both the homogeneous and heterogeneous permeability cases (Figure 7b). With decreased sediment permeability, simulated surface heat flow approaches the conductive case for all simulations, and simulated recharge and the standard deviation of surface heat flow approach zero (Figures 6, 7).

Second, I consider the role of basement permeability in influencing simulated surface heat flow (as noted above, basement is defined as the Salinian Granite, Franciscan Assemblage, and Great Valley Sequence). Simulated surface heat flow in the Coast Ranges is only affected by the choice of basement permeability at locations where the sediment-basement contact is less than 2 km deep (between approximately 40 and 64 km along the profile) (Figure 6). The maximum difference in simulated surface heat flow for the two choices of basement permeability is ~ 20 mW/m^2 for sediment permeability of 10^{-15} m^2, but is generally less than this and is localized to a small region. Further to the northeast along the profile, the maximum difference in surface heat flow between the cases of high-permeability and low-permeability basement is ~ 50 mW/m^2 for sediment permeability of 10^{-15} m^2, and is attributed to an outcrop of Great Valley Sequence between positions 64 and 74 km. Incorporation of high-permeability basement increases the standard deviation of simulated surface heat flow in the Coast Ranges by less than 4 mW/m^2 and simulated mean recharge by less than 0.08 cm/yr compared with simulations incorporating low-permeability basement (Table 3, Figure 7). For permeabilities of the Tertiary sediments between 3×10^{-16} and 4×10^{-16} m^2, the standard deviation of simulated surface heat flow is similar to the standard deviation of the heat flow data for both choices of basement permeability (Figure 7a). As noted above, these permeabilities are consistent with measured values of sediment permeability in the study area (Table 2).

Because advection of heat by groundwater flow results in decreased surface heat flow at recharge zones and increased surface heat flow at discharge zones, it is also useful to consider surface heat flow as a function of elevation as a way to compare patterns of heat flow in the data and in simulation output. I find that simulated surface heat flow is highly sensitive to elevation for sediment permeabilities > 10^{-16} m^2 (Figure 8). For sediment permeability of 10^{-15} m^2, simulated surface heat flow in the Coast Ranges ranges between ~ 30 and 115 mW/m^2 over an elevation span of only ~ 500 m (from 200 m to 700 m) (Figure 8), for simulations including low-permeability basement. In contrast, for sediment permeability of 10^{-16} m^2, simulated surface heat flow only ranges between ~75 and 80 mW/m^2 over the entire ~ 1000 m range in elevation represented in the model (Figure 8). The heat flow – elevation relationship observed in the Parkfield heat flow dataset is similar to the heat flow-elevation relationship resulting from simulated surface heat flow for sediment permeabilities between 3×10^{-16} and 10^{-15} m^2 (Figure 8).

Variability in simulated surface heat flow at a given separation distance is also increased with higher sediment permeabilities (Figure 9). For sediment permeability of 10^{-15} m^2, simulated surface heat flow varies by as much as ~ 85 mW/m^2 over distances of 10 km. This maximum variability is decreased to ~ 30 mW/m^2 and ~ 10 mW/m^2 over distances of 10 km for sediment permeability of 3×10^{-16} and 10^{-16} m^2, respectively. Peak variability in simulated surface heat flow, which is more distinct for higher sediment permeabilities, occurs over separation distances in intervals of ~ 5 and 10 km, corresponding to typical distances between local topographic highs and lows, where heat flow is most influenced by advection. The relationship between heat flow and separation distance in the Parkfield heat flow dataset is similar to that of simulated surface heat flow for sediment permeabilities ≥ 3×10^{-16} m^2 (Figure 9).

Third, I examine the effects of San Andreas Fault zone permeability architecture on simulated surface heat flow. Fluid and heat transport through the fault zone affects surface heat flow only within ~ 10 km of the fault trace (Figure 10). For sediment permeability of 10^{-16} m^2 and a fault damage zone that is an order of magnitude more permeable than the surrounding country rock, surface heat flow is ~ 5 mW/m^2 higher and 15 mW/m^2 lower within this 10 km wide zone than for the case without a fault zone (Figure 10b). For the case of a low-permeability fault core within the damage zone, the simulated surface heat flow is nearly indistinguishable from the case without a fault zone (Figure 10b). For a fault damage zone that is two orders of magnitude more permeable than the country rock, simulated surface heat flow approaches a low of 0 mW/m^2 (for the case of a conduit) and ~ 40 mW/m^2 (for the case including a low-permeability core), and a high nearly equal to that without a fault zone (Figure 10c). The heat flow minima adjacent to the SAF generated in these simulations extends 1-2 km farther to the northeast than the heat flow minima generated in the case of a damage zone that is only one order of magnitude more permeable than the adjacent country rock. Although fault zone permeability architecture has a large effect on simulated surface heat flow close to the fault, it has a negligible effect on regional surface heat flow, which is dominantly controlled by the permeability of the Tertiary sediments.

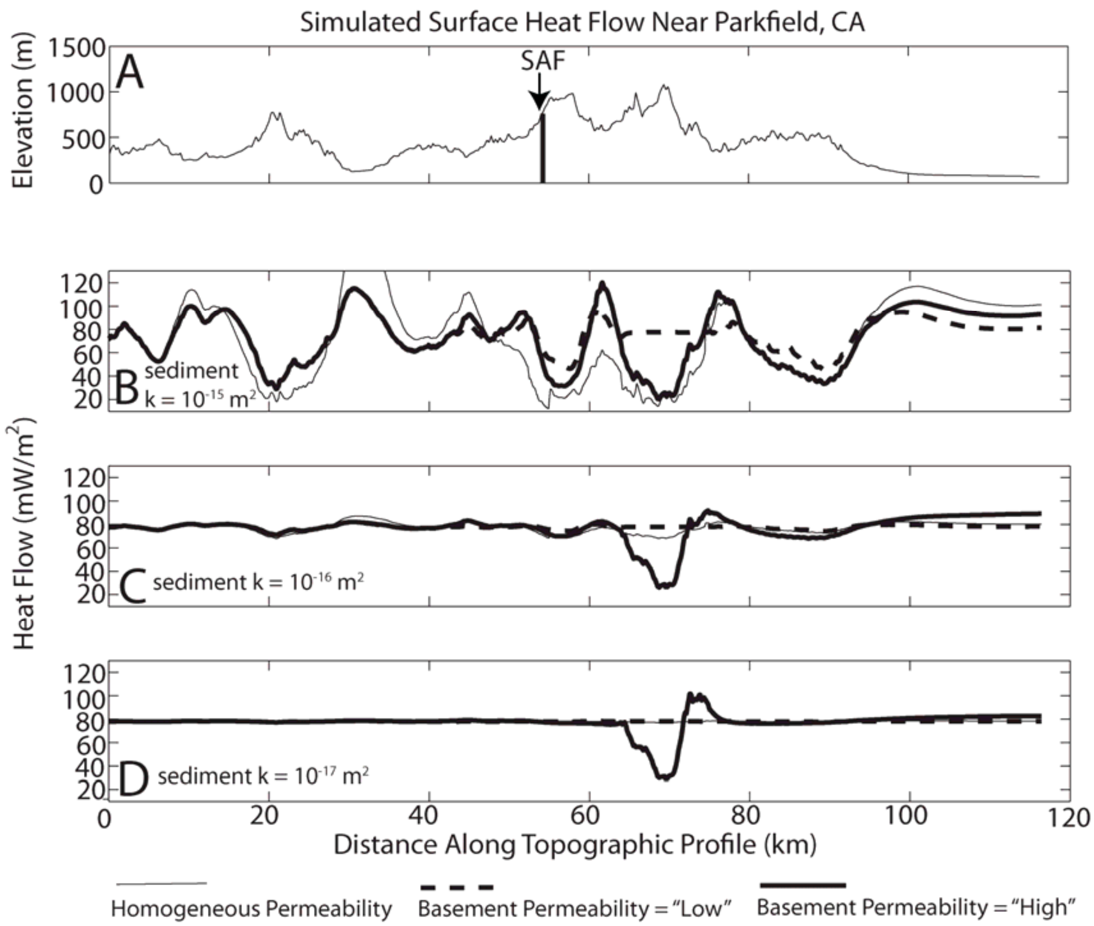

Figure 6

(A) Topographic profile used in the Parkfield model. Simulated surface heat flow (B-D) as a function of position along the profile for the cases of homogeneous permeability (thin solid line), low permeability basement (dashed line), and high permeability basement (thick solid line) for (B) sediment $k = 10^{-15}$ m^2, (C) sediment $k = 10^{-16}$ m^2, and (D) sediment $k = 10^{-17}$ m^2.

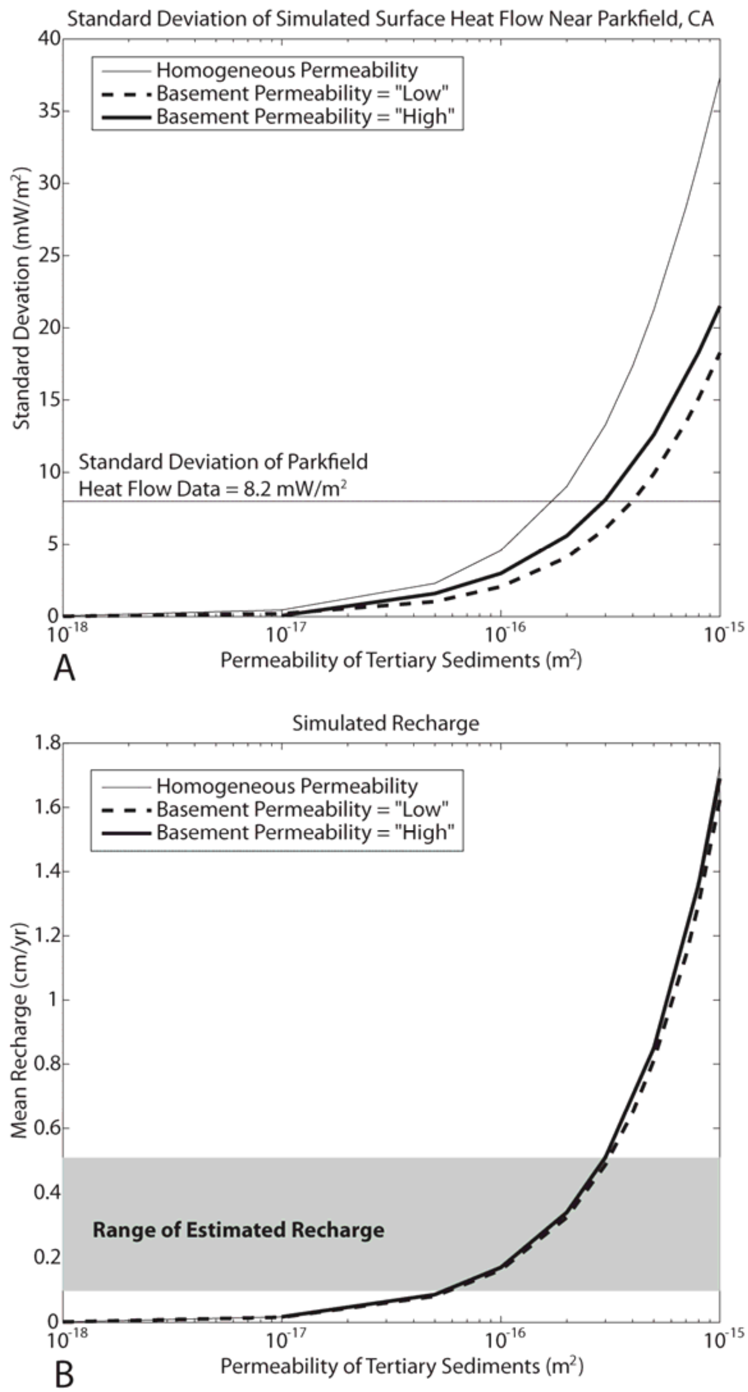

Figure 7

(A) Standard deviation of simulated surface heat flow and (B) simulated mean recharge at Parkfield for the cases of homogeneous permeability (thin solid line), low permeability basement (dashed line), and high permeability basement (thick solid line). Gray region displays range of mean recharge estimated in this study using spring data.

Table 3. Standard Deviation of Simulated Surface Heat Flow, and Simulated Recharge [a]

Simulation	PERMEABILITY (m^2) Tertiary Sediments	Salinian block	Franciscan Assemblage	Great Valley Sequence	Standard Deviation (mW/m^2)	Recharge (cm/yr)
1	10^{-15}	low	low	low	18.3	1.62
2	10^{-15}	high	high	high	21.5	1.69
3	8×10^{-16}	low	low	low	15.1	1.30
4	8×10^{-16}	high	high	high	18.3	1.36
5	5×10^{-16}	low	low	low	9.9	0.81
6	5×10^{-16}	high	high	high	12.6	0.85
7	3×10^{-16}	low	low	low	6.1	0.49
8	3×10^{-16}	high	high	high	8.1	0.51
9	10^{-16}	low	low	low	2.1	0.16
10	10^{-16}	high	high	high	3.0	0.17
11	10^{-17}	low	low	low	0.2	0.02
12	10^{-17}	high	high	high	0.8	0.02

[a] Results are from simulations not incorporating separate fault zone permeability architecture

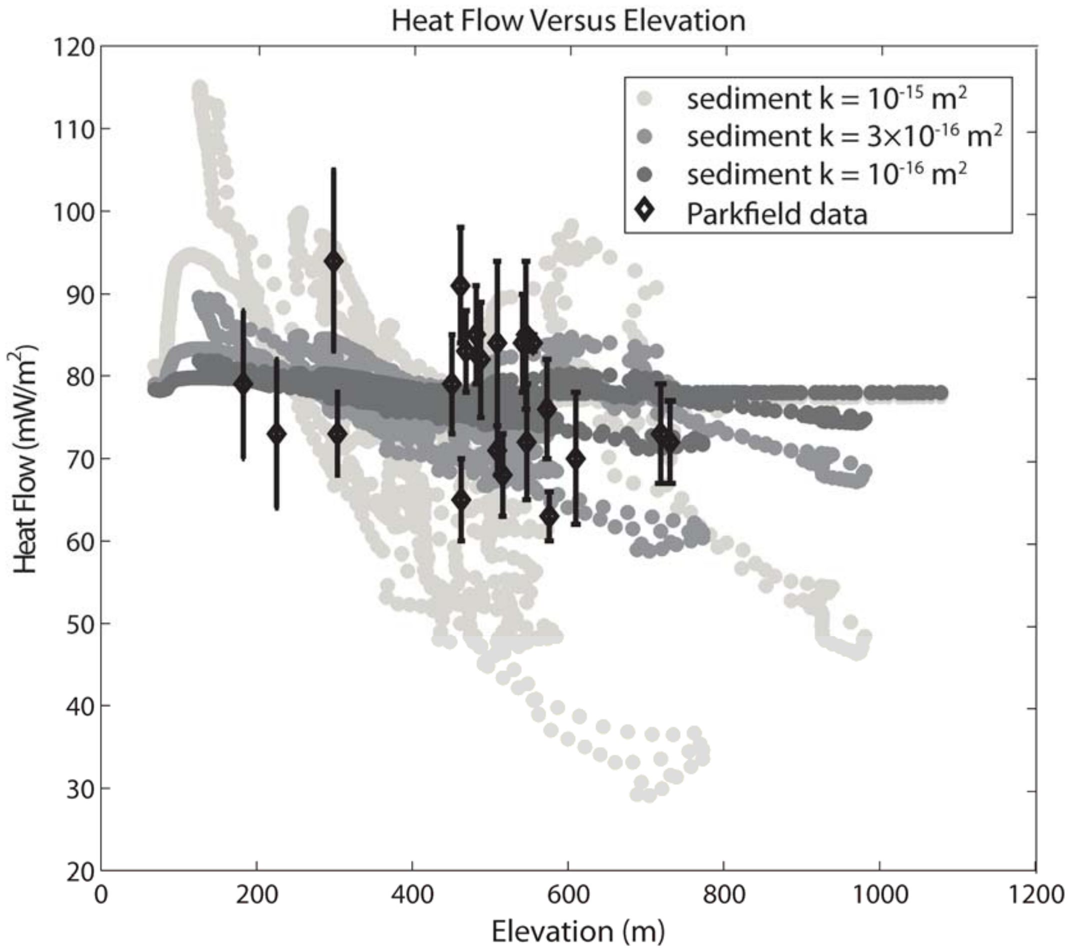

Figure 8

Observed and simulated relationship between surface heat flow and elevation, for a range of Tertiary sediment permeability, for simulations including a low-permeability basement.

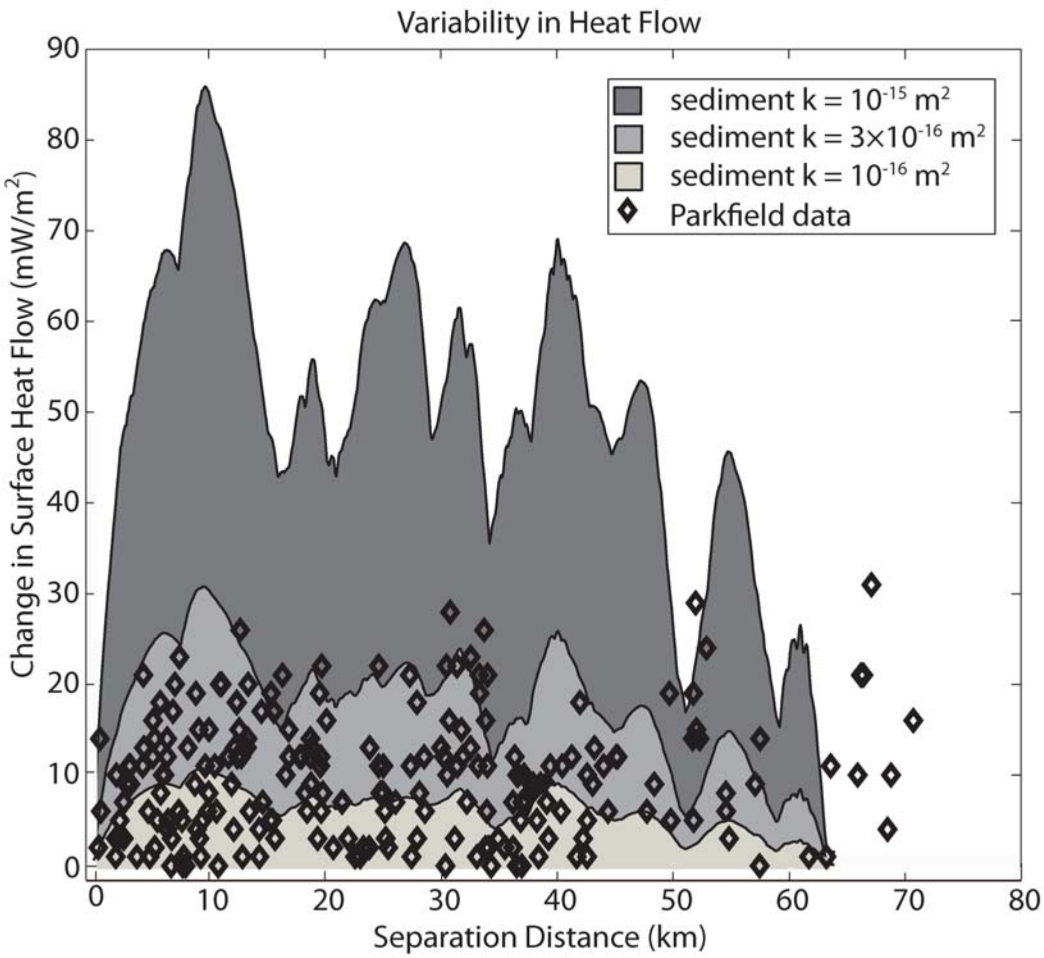

Figure 9

Observed and simulated relationship between separation distance and variability in surface heat flow for a range of Tertiary sediment permeability, for the case of a low-permeability basement. In the model, separation distance is the distance between any two locations on the topographic surface along the model profile. In the Parkfield dataset, separation distance is the great-circle distance between any two data points in map view. The apparent decrease in simulated variability with increasing separation distance is a result of having fewer pairs of simulated surface heat flow values at each subsequent higher value of separation distance in a model of finite length.

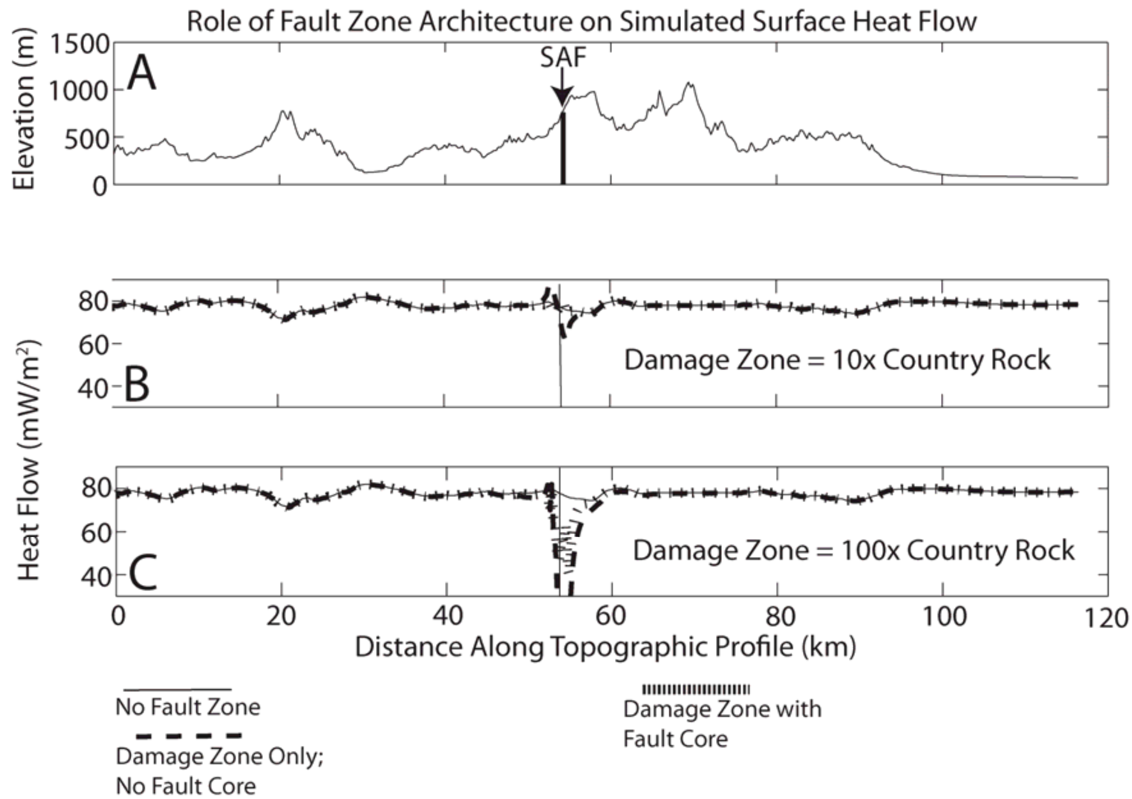

Figure 10

(A) Topographic profile used in the Parkfield model. Simulated surface heat flow (B-C) as a function of position along the profile, for sediment *k* of 10^{-16} m^2 and a low permeability basement, for (B) Damage Zone *k* = 10 times greater than that of the country rock, and (C) Damage Zone *k* = 100 times greater that of the country rock.

Fourth, I examine the effects of permeability anisotropy in the Tertiary sediments. For a given value of vertical sediment permeability, as anisotropy increases, the overall variability in simulated surface heat flow increases (Figures 11 and 12a), but variations in surface heat flow over distances of less than 5 km are subdued (Figure 11). For $k_v = 10^{-15}$ m^2, the standard deviation of simulated surface heat flow is 18.3, 29.7 and 31.4 mW/m^2 , and simulated mean recharge is 1.62, 3.7, and 5.18 cm/yr for anisotropy of 1, 5 and 10, respectively (Figure 12). In contrast, for $k_v = 10^{-16}$ m^2, standard deviation of simulated surface heat flow for these anisotropy ratios is less than 1 mW/m^2, and simulated mean recharge is less than 0.6 cm/yr for all simulations. The standard deviation of simulated surface heat flow is similar to that in the Parkfield dataset for vertical sediment permeabilities between 2×10^{-16} m^2 and 4×10^{-16} m^2, depending on anisotropy ratios, for ratios of 1-10.

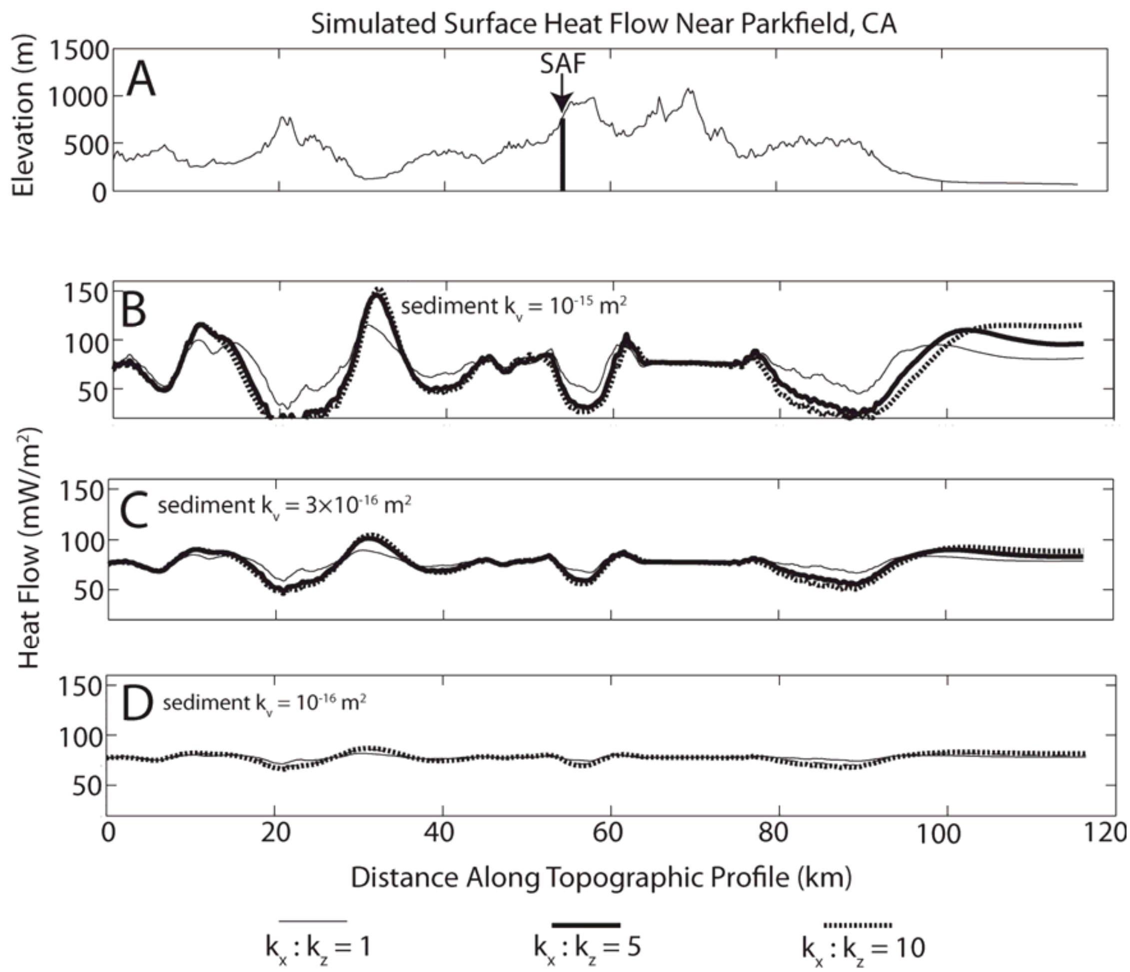

Figure 11

A.) Topographic profile used in the Parkfield model. Simulated surface heat flow (B-D) as a function of position along the profile for permeability anisotropy ratios of 1 (thin solid line), 5 (thick solid line), and 10 (dotted line) in the Tertiary sediments, including a low permeability basement and (B) sediment $k_v = 10^{-15}$ m^2, (C) sediment $k_v = 3\times10^{-16}$ m^2, and (D) sediment $k_v = 10^{-16}$ m^2.

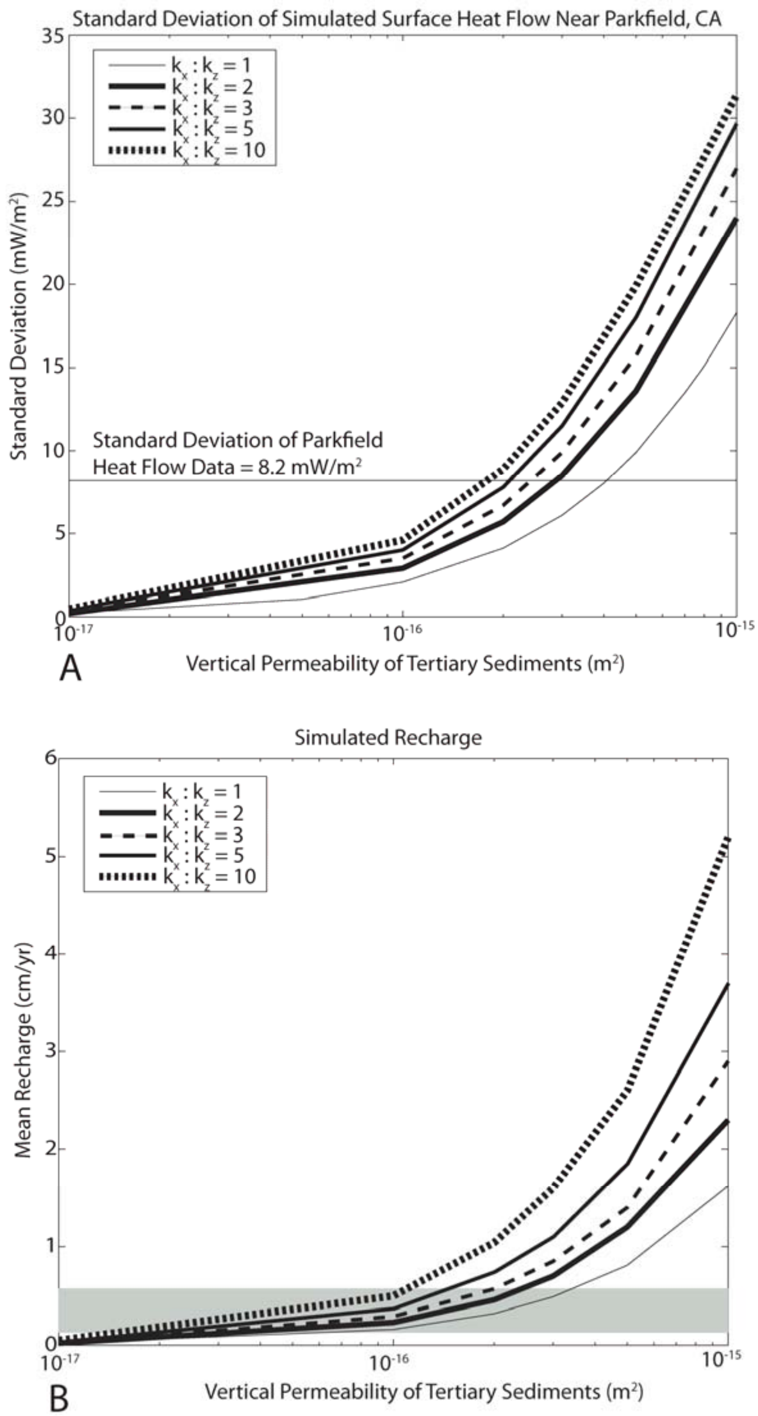

Figure 12

(A) Standard deviation of simulated surface heat flow and (B) simulated mean recharge for permeability anisotropy ratios of 1 (thin solid line), 2 (thin dashed line), 3 (thick dashed line), 5 (thick solid line), and 10 (dotted line) in the Tertiary sediments, including a low-permeability basement. Gray region displays range of mean recharge estimated in this study using spring data.

4.2 Western Mojave Desert

Simulated surface heat flow in the western Mojave Desert is generally not sensitive to the permeability of the Tertiary sediments, and remains nearly uniform and equal to the basal heat flux of 63 mW/m^2 for all sediment permeabilities $\leq 10^{-14}$ m^2 (Figure 13). Simulated surface heat flow displays variability for sediment permeability of 10^{-13} m^2, most significantly adjacent to the topographic high associated with the San Gabriel Mountains and SAF, where simulated surface heat flow is ~ 40 mW/m^2 lower than the basal heat flux (Figure 13b). For sediment permeability ranging from 10^{-15} to 10^{-13} m^2, the standard deviation of simulated surface heat flow in the western Mojave Desert NE of the SAF ranges from 0.1 to 10.6 mW/m^2 and simulated mean recharge ranges from 0.08 to 1.71 cm/yr (Figure 14). The standard deviation of simulated surface heat flow is comparable to that in the dataset for sediment permeability of ~ 4×10^{-14} m^2, corresponding to a mean recharge rate of 0.7 cm/yr (Figure 14). This sediment permeability is within the range of sediment permeability calculated from measured transmissivity and hydraulic conductivity values in the study area [*Durbin*, 1978; *Sneed and Galloway*, 2000].

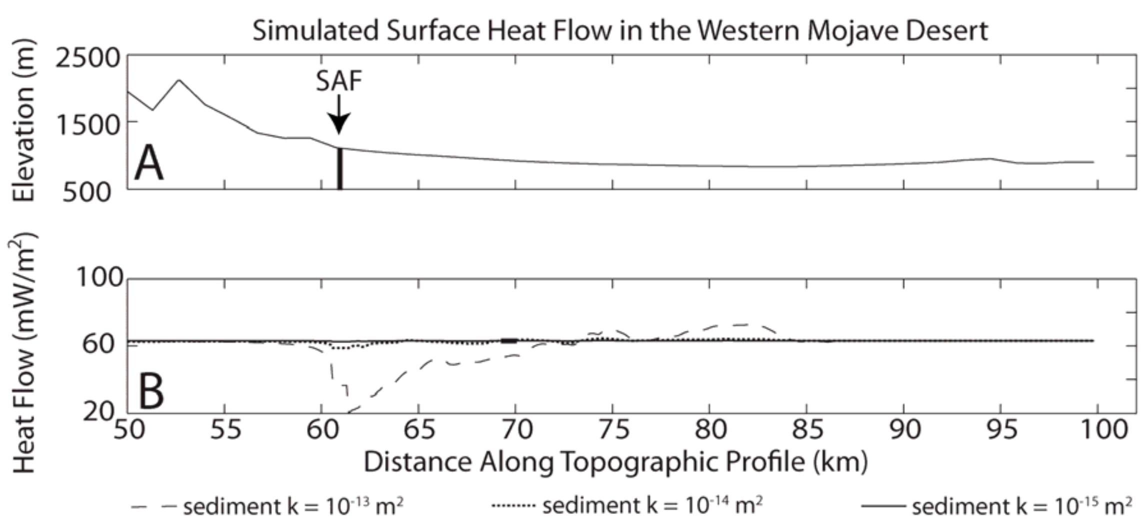

Figure 13

(A) Topographic profile used in the Mojave model and (B) simulated surface heat flow in the western Mojave Desert.

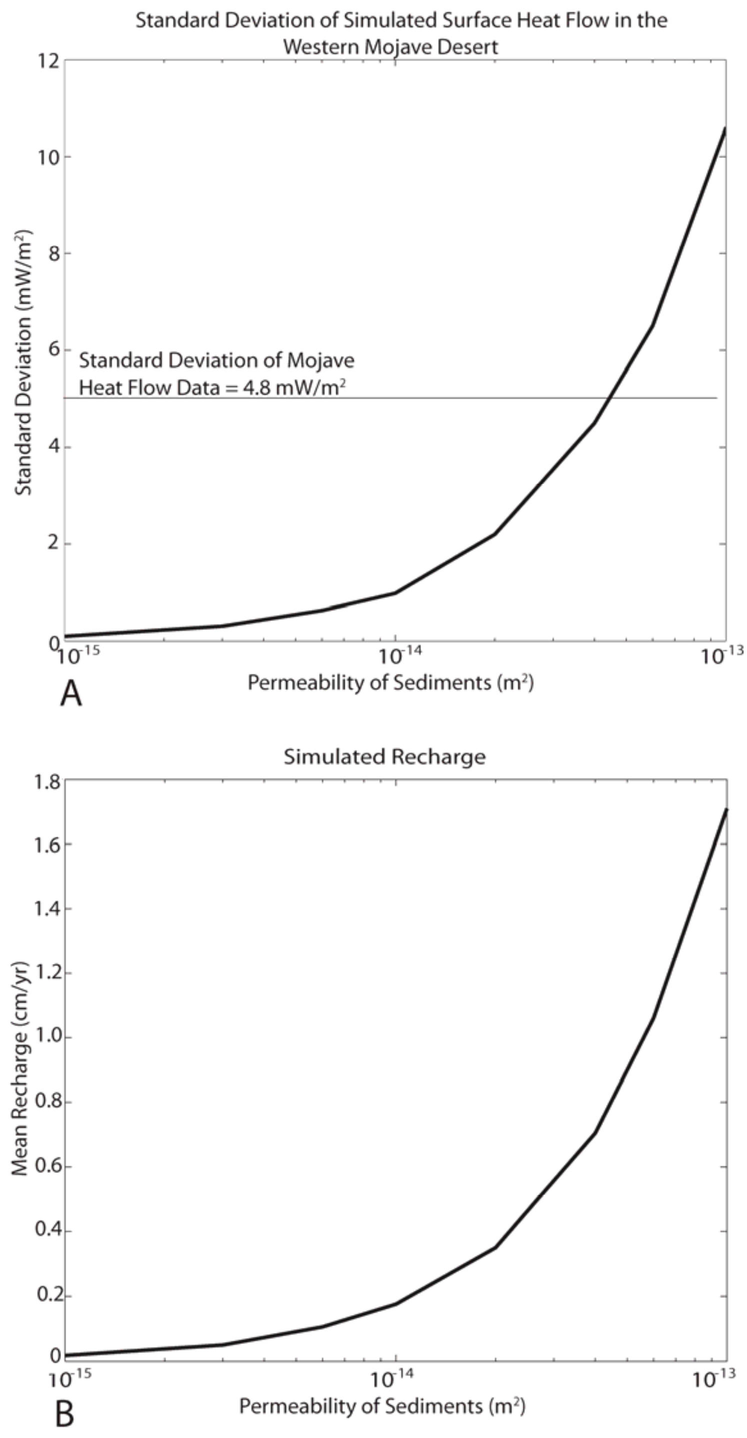

Figure 14

(A) Standard deviation of simulated surface heat flow and (B) simulated mean recharge in the western Mojave Desert

4.3 Frictional Heating on the San Andreas Fault

For the case of frictional heating on the San Andreas Fault, variability in simulated surface heat flow is related to distance from the SAF, topography, and sediment permeability (Figure 15). For sediment permeability of 10^{-17} m^2, simulated surface heat flow exhibits a broad thermal high centered at the trace of the SAF (Figure 15d), as predicted by conductive models [*Lachenbruch and Sass*, 1980; *Saffer et al.*, 2003]. For higher sediment permeabilities, the frictionally-generated heat is redistributed by advection. In these cases, simulated surface heat flow near the SAF displays maxima and minima related to topography, similar to simulations without frictional heating, but the heat flow values are shifted to higher values (Figure 15b,c).

The relationships between simulated heat flow, elevation, and proximity to the SAF in simulations including frictional heating are also clear when considering the relationship between heat flow and elevation (Figure 16). In simulations that incorporate frictional heating on the SAF, simulated surface heat flow is greater than that observed at elevations representative of those near the fault trace (500-1000 m) by ~ 30-40 mW/m^2 for sediment permeability of 10^{-15} m^2, and ~10-20 mW/m^2 for sediment permeability of 10^{-17} m^2. At elevations less than 300 m, simulated surface heat flow in the frictional heating case is not significantly different than simulated surface heat flow in the case without heating; elevations less than 300 m occur at distances > 15 km from the SAF (Figure 15a). The relationship between simulated heat flow and elevation is most similar to the relationship in the Parkfield heat flow dataset for simulations not incorporating frictional heating.

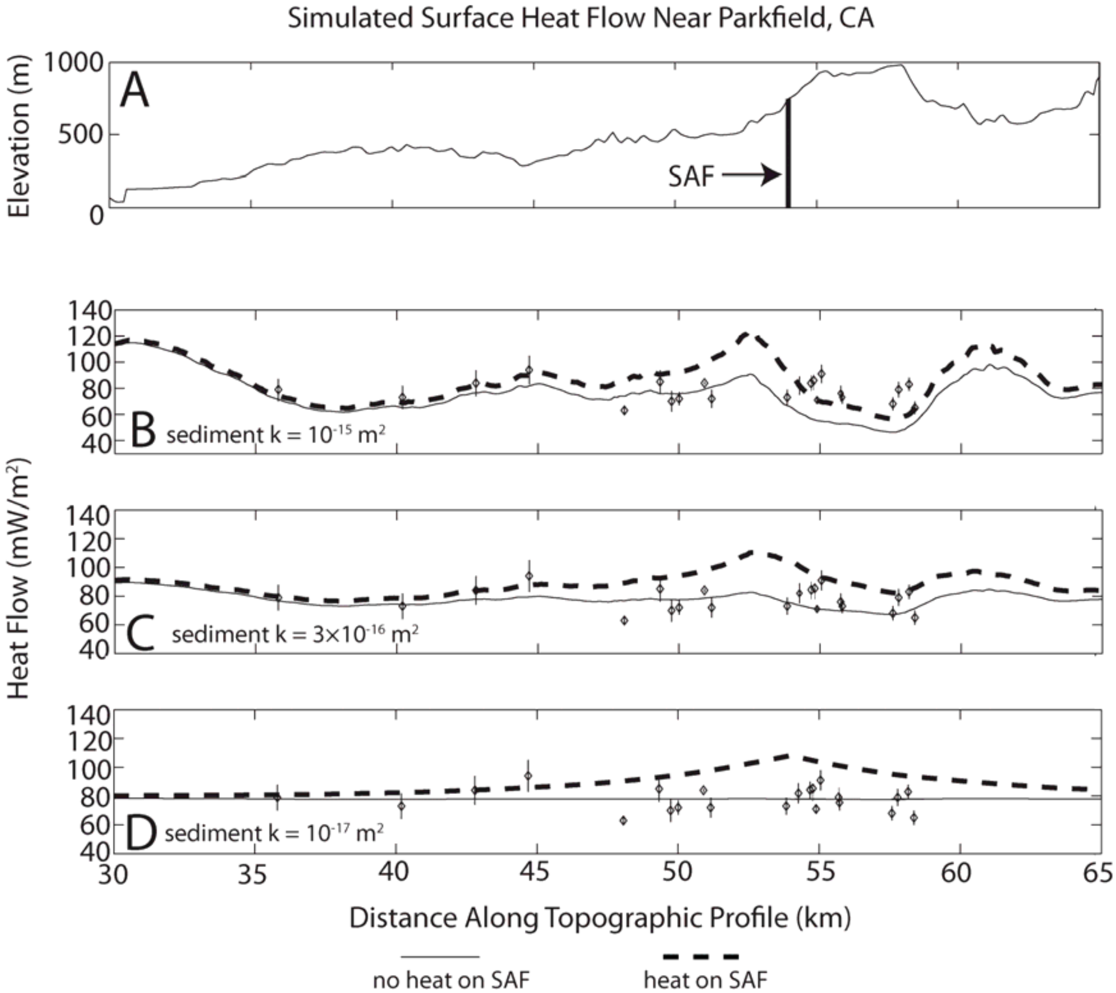

Figure 15

(A) Section of topographic profile used in the Parkfield model corresponding to the locations of the Parkfield heat flow data relative to the SAF. Simulated surface heat flow (B-D) as a function of position along the topographic profile for (B) sediment $k = 10^{-15}$ m^2, (C) sediment $k = 3\times10^{-16}$ m^2, and (D) sediment $k = 10^{-17}$ m^2 for simulations with (dashed line) and without (solid line) frictional heating on the SAF.

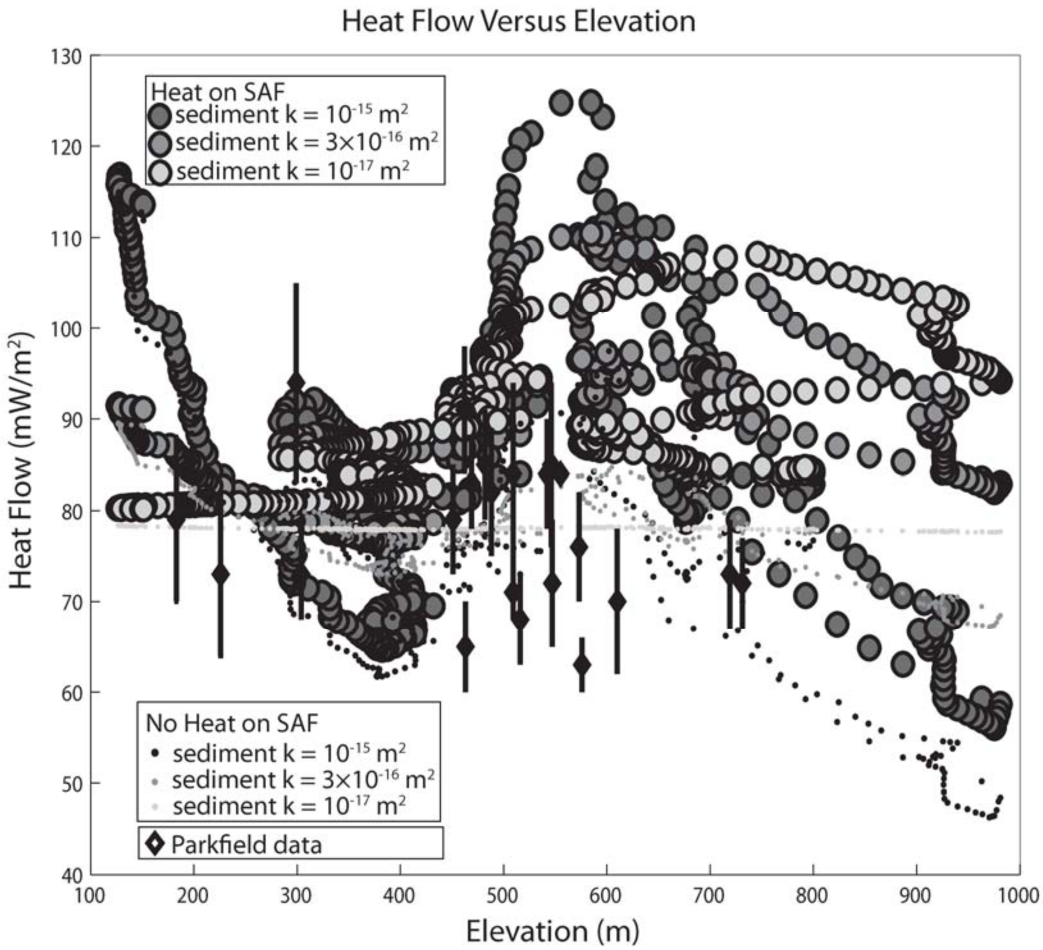

Figure 16

The simulated and observed heat flow – elevation relationship in the Parkfield heat flow data for simulations with and without frictional heating on the SAF between 20 km SW and 5 km NE of the SAF. I restrict the analysis to the section of the topographic profile corresponding to locations of the heat flow data relative to the SAF because in these simulations the characteristics of simulated surface heat flow partly depends on proximity to the SAF.

5. Discussion

5.1 Impact of Heterogeneous Permeability on Surface Heat Flow

The reduced variability in simulated surface heat flow for a heterogeneous permeability subsurface compared with the homogeneous permeability case results from decreased permeability beneath the Tertiary sediments in the basement. This limits the depth of groundwater circulation, reducing the depth and extent to which the simulated temperature field is influenced by advection [e.g., *Smith and Chapman*, 1983]. This reduction in variability is highest for high values of sediment permeability, because the permeability contrast between the Tertiary sediments and the basement is greatest relative to the homogeneous permeability case. For each model, the permeability of the sediments is the dominant control on the variability in simulated surface heat flow.

The geometry of the sediment-basement contact for the case of heterogeneous permeability is roughly horizontal (and parallel to the basal model boundary) in the Coast Ranges. The basement has a much lower permeability than the Tertiary sediments, and the model is hydrologically similar to a homogeneous permeability model with a shallow, fixed depth [e.g., *Freeze and Witherspoon*, 1967, *Smith and Chapman*, 1983]. Thus, the curves describing the decrease in standard deviation of surface heat flow with decreased sediment permeability in the homogeneous and heterogeneous permeability cases are similarly shaped (Figure 7a). However, the sediment-basement contact is not perfectly horizontal. Small irregularities in its geometry, coupled with high topographic relief, channels discharge into narrow zones at positions ~ 52 km and ~ 62 km along the topographic profile, increasing surface heat flow at these discharge zones compared with the homogeneous case.

Because the upper 1-3 km of the subsurface has the same permeability in both the homogeneous and heterogeneous permeability cases, and groundwater flow is driven by the same topography, recharge is nearly identical in the two cases for a given value of sediment permeability (Figure 7b). For a homogeneous permeability of 10^{-15} m^2, groundwater flow rates decrease by at least one order of magnitude from the topographic surface to the base of the model, allowing groundwater to advect heat on a larger scale in the homogeneous permeability case. However, it is the velocity at which groundwater moves through shallow basins in the model that determines the recharge rate.

In general, simulated surface heat flow in the Coast Ranges is not sensitive to basement permeability. Even for the high permeability functions I consider (Figure 5), permeability at a depth of 2 km in the Franciscan Assemblage and Salinian Granite is ≤ 10^{-16} m^2. At these permeabilities, advection is generally not a significant mode of heat transport [e.g. *Smith and Chapman*, 1983, 1985]. Hence, the sediment-basement contact is too deep in most of the Coast Ranges section of the model to maintain permeability high enough for significant groundwater flow. As a result, the system behaves similarly for either choice of basement permeability.

Simulated surface heat flow is significantly affected by basement permeability between 64 km and 74 km along the model profile, corresponding to an outcrop of Great Valley Sequence. However, the topography associated with this outcrop is a regional groundwater divide, and thus fluid flow through the Great Valley Sequence doesn't affect simulated surface heat flow to the southwest in the Coast Ranges, even if the Great Valley Sequence is assigned a permeability of 10^{-15} m^2 (Figure 6).

When a separate fault zone permeability architecture is included, fluid flow paths through the fault zone are driven by local topography, limiting the effects of heat advection through the fault zone to the ~10 km wide local groundwater basin associated with the fault (Figure 10). For the case of a damage zone that is two orders of magnitude more permeable than the adjacent rock (Figure 10b), the damage zone is more hydrologically connected with the adjacent sediments than in the case where the damage zone is only one order of magnitude more permeable than the adjacent rock; therefore, recharge into the fault zone occurs over a wider region to the northeast of the fault, and discharge is more widely distributed within the sediments immediately southwest of the fault. This inhibits a significant localized heat flow high from forming at the southwestern edge of the damage zone, despite the increased permeability there. A low permeability barrier in the fault divides the damage zone into two small, separate sub-basins, subduing the effects of the damage zone on heat transport (Figures 10b,c).

Permeability anisotropy subdues variations in simulated surface heat flow over distances of 2-3 km, because horizontal flow is favored over vertical flow, but increases overall variability when compared to the isotropic case with the same vertical permeability. The larger groundwater basins become the main recharge and discharge points in the system as flow through the smaller basins becomes dominantly horizontal, and therefore the smaller basins no longer accommodate significant recharge and discharge. For decreased values of vertical sediment permeability, the standard deviation of surface heat flow, and simulated mean recharge, approach that of the isotropic and conductive cases because low vertical permeability prevents groundwater from traveling to depth and significantly affecting the subsurface temperature field (Figure 12).

For the Mojave area, simulated surface heat flow for sediment permeability ≤ 10^{-14} is similar to the basal heat flux and does not vary significantly along the profile, due to lack of a significant driving topographic driving force northeast of the San Andreas Fault. The San Gabriel Mountains SW of the SAF create a large topographic driving force, but permeability (of this mountain block) is too low in this area to allow significant groundwater flow. The importance of the relationship between topography and permeability architecture in influencing surface heat flow is further demonstrated by comparing simulated surface heat flow in the Parkfield and Mojave study areas. Standard deviation of surface heat flow is 10.6 mW/m^2 for sediment permeability of 10^{-13} m^2 in the Mojave model (Figure 12a), but the standard deviation of simulated surface heat flow in the Parkfield model for a sediment permeability two orders of magnitude lower is approximately twice as high (Figure 7a). This demonstrates that the permeability threshold at which advection becomes significant in heat transport [e.g., *Smith and Chapman*, 1983, 1985] varies depending on subsurface permeability architecture and topographic driving force (water table configuration), and can be orders of magnitude higher than the range 7×10^{-16} m^2 to 3×10^{-16} m^2 reported for basins with simplified dimensions and hydrologic characteristics.

In addition, the results of the sensitivity analysis performed in this study demonstrate that heat flow observations from a single borehole cannot be used to determine if regional heat transport is dominantly conductive or advective [e.g., *Williams et al.*, 2004]. Causes of a conductive thermal gradient at a particular location can include: (1) low subsurface permeability and/or low topographic gradient in a heterogeneous permeability crust with significant advection occurring elsewhere, or (2) dominantly horizontal groundwater flow if the location is above an area between a recharge and discharge zone, resulting in a vertical thermal gradient that mimics a conductive case.

5.2 Comparison Between Observed and Simulated Surface Heat Flow

Simulation results for the Parkfield region with sediment permeabilities between 3×10^{-16} m^2 and 10^{-15} m^2 are consistent with the standard deviation (Figure 7a), relationship between heat flow and elevation (Figure 8), and variability in heat flow with separation distance (Figure 9) in the Parkfield heat flow dataset. This result is robust for both high and low basement permeability, and for the range of fault permeability structure. These permeabilities are within the range of those observed for the Tertiary sediments in the area [*Wylie et al.*, 1996; *Coburn and Gillespie*, 2002; *Link et al.*, 1986; *Montgomery and Morea*, 2001; *Clark et al.*, 2001] (Table 2), and correspond to mean recharge rates from 0.51 cm/yr to 1.69 cm/yr (Table 3). Although the standard deviation of simulated surface heat flow and variability in heat flow with separation distance are higher than observed for sediment permeability of 10^{-15} m^2, the heat flow data may be undersampled and thus underestimate the true variability in surface heat flow. If permeability anisotropy in the Tertiary sediments is included, the characteristics of simulated surface heat flow are consistent with those in the dataset for k_v between 2×10^{-16} m^2 and 4×10^{-16} m^2, over a range of k_x:k_v of 1-10; this corresponds to mean recharge rates from 0.51 cm/yr to 1 cm/yr. Further heterogeneity, such as additional faults, would increase overall variability in simulated surface heat flow and not affect the main conclusions of this study.

In the western Mojave Desert, simulated surface heat flow for a sediment permeability of 4×10^{-14} m^2 is consistent with the standard deviation of the heat flow data. This corresponds to a mean recharge rate of 0.7 cm/yr. This sediment permeability is within the range of sediment permeability calculated from measured transmissivity and hydraulic conductivity in the study area [*Durbin*, 1978; *Sneed and Galloway*, 2000]. However, because the advective effects associated with permeabilities $\geq 4\times10^{-14}$ m^2 are limited to the region in the model adjacent to the San Andreas Fault, the low variability in observed heat flow can be produced in either a conductive or advectively dominated scenario. However, core material in the Mojave Desert as deep as 30 m in areas away from streambeds is dry and has highly negative water potentials [*Izbicki et al.*, 2000a]. Rates of downward water infiltration estimated from chloride concentration suggest that precipitation takes at least 10,000 yr to reach 10 m in some areas [*Izbicki et al.*, 2000a], suggesting that areal groundwater recharge doesn't occur or is extremely low. Chloride and tritium data suggest that water does infiltrate to depths beyond the root zone underlying several intermittent streams, but the thick, heterogeneous unsaturated zone suggests that groundwater recharge is very slow [*Izbicki et al.*, 2000a, 2007]. These observations are most consistent with a conductively-dominated thermal regime.

5.3 Frictional Heating on the San Andreas Fault

Surface heat flow from simulations incorporating frictional heating from a "strong" SAF is not consistent with the surface heat flow data near Parkfield. In simulations incorporating heating on the SAF with sediment permeability high enough to permit significant groundwater flow (Figure 15a), a broad thermal anomaly centered at the trace of the SAF is not generated, but maximum simulated surface heat flow near the fault is ~ 10-20 mW/m^2 higher than the predicted 30-40 mW/m^2 conductive thermal anomaly, because advection amplifies the heat flow maxima already present at topographic lows (Figures 15, 16). In regions adjacent to the fault trace, it appears that simulated surface heat flow for the case of high sediment permeability and including frictional heating is consistent with the Parkfield dataset (Figure 15a). However, simulated surface heat flow is sensitive to elevation. Because the elevations of the Parkfield data points and the elevations in the topographic profile used in the model are not the same at equivalent distances from the SAF, the similarity between observed and simulated surface heat flow for high sediment permeability when simulated and observed surface heat flow is displayed as a function of distance along the model profile (Figure 15a) cannot be used to suggest that it is possible for a frictionally-generated thermal anomaly at the trace of the SAF to be masked by groundwater flow. At intermediate elevations (~ 400-600 m) in the vicinity of the fault, simulated surface heat flow for the case of frictional heating for all values of sediment permeability is considerably higher than observed (Figure 16).

5.4 Constraints on Regional Recharge

Regional recharge estimates for the sparsely populated interior Coast Ranges are generally not well known, but provide an important constraint on my Parkfield model. I estimate recharge for four watersheds in the Coast Ranges encompassing Kessler Springs in San Luis Obispo County, and Sulphur Spring on Mission Creek, Bane's Soda Springs, and Helm's Soda Springs in Monterey County [*Waring*, 1915] in order to compare with simulated recharge for the Parkfield area. These watersheds vary in size, topographic gradient, and rock type, and the temperature of spring discharge is atmospheric. Hot springs are not used in this study due to the possibility that fluids associated with volcanic activity at depth contribute to their discharge.

For simplicity, I assume that all water discharging from each spring originated as rainfall in the surrounding watershed, and that the groundwater and surface water basin boundaries are identical. I divide the spring discharge by the area of the watershed to obtain a recharge estimate for the basin. If the spring is only fed by a smaller portion of the watershed, for example a highly fractured zone [e.g., *Rowland et al.*, 2008], locally steep slope, or stratigraphic pinchout, then the estimated recharge rate should be considered a minimum. Similarly, if there are additional springs in the watershed that discharge water, or if the streams in the watershed have baseflow, then the recharge estimate should also be considered a minimum. Subsurface inflow or outflow into the watershed would also create uncertainty in the recharge estimate. Recharge estimates for the four watersheds range from 0.08 to 0.5 cm/yr (Table 4). This range is consistent with simulated recharge for sediment permeabilities of 5×10^{-17} to 3×10^{-16} m^2.

5.5 Recommendations for Future Work

My results demonstrate that it is possible for topographically driven groundwater flow to generate significant scatter in near-surface heat flow, when considering realistic permeability architecture in the Parkfield area. With sediment permeabilities $\geq 3\times10^{-16}$ m^2, and commensurate recharge of ~ 0.5 cm/yr, advective effects are significant enough to produce the variation and spatial characteristics of the scatter in the surface heat flow data. However, thermal refraction can also generate similar heat flow scatter in a purely conductive regime [*Fulton and Saffer*, 2009]. Because heat flow is severely

Table 4. Hydrologic Information and Recharge Estimates for Springs

Name of Spring(s)	Total Discharge [a] (m^3/yr)	Area of Watershed Upgradient (km^2)	Topographic Gradient of Watershed	Rock Type in Watershed	Recharge Estimate (cm/yr)
Kessler Springs and Springs on Onyx Marble Quarry (San Luis Obispo County)	4000	9	0.13	Tertiary Sediments	0.04
Sulphur Spring on Mission Creek (Monterey County)	9900	12	0.12	Tertiary Sediments	0.08
Bane's Soda Springs (Monterey County)	9900	2	0.41	Franciscan Assemblage	0.5
Helm's Soda Springs (Monterey County)	9900	12	0.076	Franciscan Assemblage	0.08

[a] Total discharge for each spring or group of springs is from *Waring* [1915].

undersampled relative to the geographic scale of the Coast Ranges and the subsurface geology is not precisely known through most of the region, the exact cause of the heat flow scatter in the California Coast Ranges may never be determined. In my recommendations, I focus on what can be done to quantify recharge rates in the interior Coast Ranges, to determine if advection is significant and thus a viable mechanism for generating the observed scatter in heat flow.

Understanding the regional permeability and recharge rates in groundwater basins of the interior Coast Ranges would not only be beneficial in assessing advective power, but also for understanding and managing groundwater resources in this sparsely populated area. In 2003, the California Department of Water Resources issued Bulletin 118-Update 2003, a comprehensive list of groundwater basins throughout the state including basic information on their physical boundaries, composition of basin fill and aquifer material, and source of recharge (i.e., precipitation, infiltration from creeks, etc.). Although recharge estimates exist for a subset of the permeable coastal aquifers composed of river alluvium, natural recharge estimates are unavailable for the basins of the interior Coast Ranges, composed largely of moderately-consolidated sediments overlying basement.

The best option for quantifying recharge rates in the interior Coast Ranges may be to drill wells and perform a chemical and isotopic analysis of groundwater for several groundwater basins that are both typical of those in the Coast Ranges and have well-defined boundaries, recharge, and discharge zones, or the potential to define these boundaries and zones with fieldwork. The geometries and thicknesses of lithologic units in the basins could be inexpensively and quickly delineated with gravity modeling aided by well control, provided there are sufficient density contrasts between basin fill and bedrock [e.g., *Griscom and Jachens*, 1990, and references therein]. Given information about the isotopic composition of precipitation in a particular basin, which may vary with elevation and distance from the Pacific Ocean, $\delta^{18}O$ and $\delta^{2}H$ values could potentially be used to trace the path of groundwater flow in a basin and determine structural characteristics that may influence flow [e.g., *Wood and Sanford*, 1995; *Izbicki et al.*, 2007]. Chloride concentrations in groundwater that are well-defined over a single basin could be used to date water along the flow paths and provide estimates of recharge [e.g., *Wood and Sanford*, 1995, *Scanlon*, 1991]. The spatial variability in concentration could be used in conjunction with a numerical model coupling flow and chemical transport to estimate flow and recharge rates. However, connate water derived from the Great Valley Sequence and fluids associated with metamorphic dehydration of the Franciscan Assemblage contribute to the isotopic signature of groundwater [e.g., *Peters*, 1993], and thus basins underlain by granitic basement would be better choices for such an approach. Due to the high local variability in spring water and isotopic composition in California [e.g., *Kharaka et al.*, 1988; *Rowland et al.*, 2008], springs probably do not adequately represent bulk groundwater chemistry in the subsurface, requiring water sampling from wells for the chemical analyses described above. Comparison of groundwater and water composition from nearby springs could assess whether spring chemistry is representative of the regional groundwater.

Estimating recharge using spatial and seasonal variations in channel flow is not practical in the Coast Ranges because most streams have been heavily altered for human uses [*USGS*, streamflow data and descriptions]. Due to the complexities of estimating recharge rates in semi-arid environments, it might be beneficial to first estimate how much water actually infiltrates beyond the root zone in numerous groundwater basins in the Coast Ranges by examining the tritium and chloride profiles in the unsaturated zone at suspected recharge zones, including streambeds [e.g., *Wood and Sanford*, 1995; *Izbicki et al.*, 2007]. If infiltration rates are low, it may be unrealistic to still consider the possibility that mean regional recharge in the Coast Ranges is ~ 0.5 cm/yr. Another option would be to obtain more values of surface heat flow in areas of well-defined geology, particularly at the upper and lower ranges of elevation, where simulated surface heat flow differs most between conduction and advection-dominated scenarios.

6. <u>Conclusions</u>

Previous models simulating topographically driven groundwater flow through an upper crust characterized by homogeneous permeability do not produce key features of surface heat flow scatter near Parkfield, CA. Here, I construct coupled fluid and heat transport models near Parkfield and in the western Mojave Desert and compare simulated and observed surface heat flow in these regions. These models are the first comprehensive assessment of regional groundwater and heat transport that incorporate realistic permeability architecture for the Parkfield and Mojave areas, and results of the sensitivity analysis will be useful to hydrogeologists modeling fluid and heat transport in regions with complex hydrologic characteristics and topography. I find that the permeability of the Tertiary sediments that comprise the upper 3 km in the Parkfield area is the main influence on patterns and scatter of simulated surface heat flow. The reduced depth of groundwater circulation created by the contact between the Tertiary sediments and low-permeability basement below causes decreased variability in simulated surface heat flow compared with that generated under the assumption of homogeneous permeability [*Saffer et al.*, 2003; *Fulton et al.*, 2004]. This result is not sensitive to basement permeability, which affects the variability in simulated surface heat flow only slightly, and only in locations where the sediment-basement contact is less than 2 km beneath the land surface. Likewise, heat advection through a permeable SAF zone creates very localized variations in surface heat flow relative to the scale of the study area. Permeability anisotropy significantly increases variability in simulated surface heat flow, but only for vertical sediment permeabilities greater than those that produce the characteristics of the heat flow scatter (Table 2).

Simulated surface heat flow is consistent with observed surface heat flow in the Parkfield area if the permeability of the upper 2-3 km of the crust is between 3×10^{-16} m^2 and 10^{-15} m^2, with an associated mean recharge rate of ~ 0.5 cm/yr. Topographically driven groundwater flow through a heterogeneous permeability subsurface cannot both mask a thermal anomaly at the trace of the SAF and also generate the observed characteristics of the scatter in the dataset. Simulations that generate heat flow scatter consistent with that in the data predict heat flow that is significantly higher than observed at elevations associated with the San Andreas Fault, for both advective and conductive scenarios (Figure 16). Thus, although there are arguments for both a weak and strong fault [e.g., *Scholz* 2000], the surface heat flow data in the California Coast Ranges is most consistent with a weak fault when the effects of advection through a realistic, heterogeneous permeability upper crust are considered.

In the western Mojave Desert, simulated surface heat flow is not significantly influenced by advection for sediment permeability ≥ 10^{-14} m^2, due to the lack of a significant topographic driving force, and the nearly constant observed surface heat flow is consistent with sediment permeabilities up to 10^{-13} m^2. However, recharge estimates suggest that groundwater flow is minimal and heat is transported dominantly by conduction, regardless of sediment permeability. High permeability or high topographic gradients alone are not sufficient to produce advective effects in surface heat flow, and in cases where the topographic driving force is small, the onset of significant advective heat transport can occur at permeabilities significantly higher than 7×10^{-16} m^2 and 3×10^{-16} m^2 reported for generic basins with homogeneous hydrologic properties [e.g., *Smith and Chapman* 1983, 1985].

Given the relationships between topography and geologic architecture in the California Coast Ranges, it is possible for topographically driven groundwater flow through a heterogeneous permeability upper crust to generate the characteristics of the surface heat flow scatter near Parkfield. However, the similarity between the characteristics of simulated and observed surface heat flow does not imply that groundwater flow is actually influencing surface heat flow in this region or that the regional permeability of the upper 2-3 km of the subsurface is indeed high enough to permit mean recharge of 0.5 cm/yr, as the scatter in surface heat flow can also be generated in a purely conductive regime by thermal refraction [*Fulton and Saffer*, 2009]. Although recharge rates in the interior Coast Ranges are not well known, groundwater flow is a regional-scale process capable of producing short-wavelength variability in surface heat flow. Thus, until the characteristics of regional groundwater flow in the interior California Coast Ranges are better quantified, topographically driven groundwater flow must be considered as a potential contributor to the heat flow signature in the Coast Ranges and viewed as a potential limitation when using surface heat flow to quantify tectonic conditions at depth.

References

Bartow, J. A. (1990), A Summary of the Cenozoic stratigraphy and geologic history of the Coalinga region, Central California, in *The Coalinga, California, earthquake of May 2, 1983*, edited by M. J. Rymer and W. L. Ellsworth, *Prof. Pap.*, *1487*, 3-12, U.S. Geol. Surv., Reston, VA.

Becken, M., O. Ritter, S. K. Park, P. A. Bedrosian, U. Weckmann, and M. Weber (2008), A deep crustal fluid channel into the San Andreas Fault system near Parkfield, California, *Geophys. J. Int.*, *173*(2), 718-732, doi: 10.1111/j.1365-246X.2008.03754.x.

Becker, M. W., T. Georgian, H. Ambrose, J. Siniscalchi, and K. Frederick (2004), Estimating flow and flux of groundwater discharge using water temperature and velocity, *J. Hydrol.*, *296*(1-4), 221-233, doi: 10.1016/j.jhydrol.2004.03.025.

Bennington, N., C. Thurber, and S. Roecker (2008), Three-dimensional seismic attenuation structure around the SAFOD Site, Parkfield, California, *Bull. Seismol. Soc. Am.*, *98*(6), 2934-2947, doi: 10.1785/0120080175.

Blackwell, D. D., J. L. Steele, and C. A. Brott (1980), The terrain effect on terrestrial heat flow, *J. Geophys. Res.*, *85*(B9), 4757-4772, doi: 10.1029/JB085iB09p04757.

Blackwell, D. D., R. G. Bowen, D. A. Hull, J. Riccio, and J. L. Steele (1982), Heat flow, arc volcanism, and subduction in northern Oregon, *J. Geophys. Res.*, *87*(B10), 8735-8754, doi: 10.1029/JB087iB10p08735.

Bodvarsson, G. S., E. M. Kwicklis, C. Shan, and Y. Wu (2003), Estimation of percolation flux from borehole temperature data at Yucca Mountain, Nevada, *J. Contam. Hydrol.*, *62-63*, 3-22, doi: 10.1016/S0169-7722(02)00178-X.

Boness, N. L., and M. D. Zoback (2004), Stress-induced seismic velocity anisotropy and physical properties in the SAFOD pilot hole in Parkfield, CA, *Geophys. Res. Lett.*, *31*(15), L1517, doi: 10.1029/2003GL019020.

Boness, N. L., and M. D. Zoback (2006), A multiscale study of the mechanisms controlling shear velocity anisotropy in the San Andreas Fault Observatory at Depth, *Geophysics*, *71*(5), F131-F146, doi: 10.1190/1.2231107.

Bouri, S., I. B. Abdallah, Y. Zarhloule, H. B. Dhia, and B. Hamed (2007), Thermal regime, groundwater flow, and petroleum occurrences in the Cap Bon region, northeastern Tunisia, *Geothermics*, *36*(4), 362-381, doi: 10.1016/j.geothermics.2007. 05.002.

Brace, W. F (1980), Permeability of crystalline and argillaceous rocks, *Int. J. Rock Mech. Min. Sci. Geomech. Abstr.*, *17*(5), 241-251.

Brace, W. F., and D. L. Kohlstedt (1980), Limits on lithospheric stress imposed by laboratory experiments, *J. Geophys. Res.*, *85*(B11), 6248-6252, doi: 10.1029/ JB08 5iB11p06248.

Bradbury, K. K., D. C. Barton, J. G. Solum, S. D. Draper, and J. P. Evans (2007), Mineralogical and textural analyses of drill cuttings from the San Andreas Fault Observatory at Depth (SAFOD) boreholes; initial interpretations of fault zone composition and constraints on geologic models, *Geosphere*, *3*(5), 299-318, doi: 10.1130/GES00076.1.

Bradbury, K. K., T. Jeppson, J. P. Evans, J. Chester, and F. Chester (2008), Preliminary geological and geophysical analyses of phase 3 core, San Andreas Fault Observatory at Depth borehole (SAFOD), Parkfield, California, *Geol. Soc. Am. Abstracts with Programs*, *40*(6), 150.

Bridges, R. A., and J. W. Castle (2003), Local and regional tectonic control on sedimentology and stratigraphy in a strike-slip basin; Miocene Temblor Formation of the Coalinga area, California, USA, *Sediment. Geol.*, *158*(3-4), 217-297, doi: 10.1016/ S0037-0738(02)00314-7.

Brocher, T. M., A. L. Rubel, T. L. Wright, and D. A. Okaya (1988), Compilation of 20 sonic and density logs from 12 oil test wells along LARSE lines 1 and 2 in the Los Angeles basin, California, *Open-File Report, 98-366*, 53 pp., U.S. Geol. Surv., Reston, VA.

Brune, J. N., T. L. Henyey, and R. F. Roy (1969), Heat flow, stress, and rate of slip along the San Andreas Fault, California, *J. Geophys. Res.*, *74*(15), 3821-3827.

Byerlee, J. (1978), Friction of rocks, *Pure Appl. Geophys.*, *116*(4-5), 615-626.

Calcagno, P., C. Baujard, A. Dagallier, T. Kohl, G. Courrioux, L. Guillou-Frottier, and A. Genter (2008), The Limagne geothermal reservoir (France); from 3D geological model to potential assessment, *Int. Geol. Congress Abstracts*, *33*, 1319666.

California Department of Water Resources (2003), California's Ground Water, *Bulletin 118-Update 2003*.

Chester, J. S., F. M. Chester, D. Kirschner, J. P. Evans, D. W. Sills, and C. G. Coble (2008), Structure of the San Andreas fault zone at SAFOD, *Geol. Soc. Am. Abstracts with Programs*, *40*(6), 150.

Clark, M. S., L. F. Klonskey, and K. E. Tucker (2001), Geologic study and multiple 3-D surveys give clues to complex reservoir architecture of giant Coalinga oil field, San Joaquin Valley, California, *Leading Edge*, *20*(7), 746-751.

Coburn, M. E., and J. M. Gillespie (2002), A hydrogeologic study to optimize steamflood performance in a giant oilfield; Kern River Field, California, *AAPG Bull.*, *86*(8), 1489-1505, doi: 10.1306/61EEDCD8-173E-11D7-8645000102C1865D.

Coyle, B. J., and M. D. Zoback (1988), In situ permeability and fluid pressure measurements at 2 km depth in the Cajon Pass research well, *Geophys. Res. Lett.*, *15* (9), 1029-1032, doi: 10.1029/GL015i009p01029.

Crawford, B. R., D. R. Faulkner, and E. H. Rutter (2008), Strength, porosity, and permeability development during hydrostatic and shear loading of synthetic quartz-clay fault gouge, *J. Geophys. Res.*, 113(B3), B03207, doi: 10.1029/2006JB004634.

Dahl-Jensen, D., K. Mosegaard, N. Gundestrup, G. D. Clow, S. J. Johnsen, A. W. Hansen, and N. Balling (1998), Past temperatures directly from the Greenland ice sheet, *Science*, *282*, 268-271.

D'Alessio, M. A., C. F. Williams, and R. Burgmann (2006), Frictional strength heterogeneity and surface heat flow; implications for the strength of the creeping San Andreas Fault, *J. Geophys. Res.*, *111*(B5), B05410.

David, C., T. Wong, W. Zhu, and J. Zhang (1994), Laboratory measurement of compaction-induced permeability change in porous rocks; implications for the generation and maintenance of pore pressure excess in the crust, *Pure Appl. Geophys.*, *143*(1-3), 425-456.

Davis, S. N. (1969), Porosity and permeability of natural materials, in *Flow through Porous Media*, edited by R. J. M. De Wiest, pp. 53-89, Academic Press, New York-London.

Dholakia, S. K., A. Aydin, D. D. Pollard, and M. D. Zoback (1998), Fault-controlled hydrocarbon pathways in the Monterey Formation, California, *AAPG Bull.*, *82*(8), 1551-1574.

Dibblee, T. W., Jr. (1973), Regional geologic map of San Andreas and related faults in Carrizo Plain, Temblor, Caliente, and La Panza ranges and vicinity, California, *Miscellaneous Geologic Investigations Map. 0757*, U.S. Geol. Surv., Reston, VA.

Dickinson, W. R. (1966), Structural relationships of San Andreas Fault system, Cholame Valley and Castle Mountain Range, California, *Geol. Soc. Am. Bull.*, *77*(7), 707-726, 10.1130/0016-7606(1966)77[707:SROSAF]2.0.CO;2.

Dickinson, W. R., and E. I. Rich (1972), Petrologic intervals and petrofacies in the Great Valley Sequence, Sacramento Valley, California, *Geol. Soc. Am. Bull.*,*83*(10), 3007-3024, doi: 10.1130/0016-7606(1972)83[3007:PIAPIT] 2.0.CO;2

Ducea, M., M. A. House, and S. Kidder (2003), Late Cenozoic denudation and uplift rates in the Santa Lucia Mountains, California, Geology, 31(2), 139-142, doi: 10.1130/ 0091-7613(2003)031<0139:LCDAUR>2.0.CO;2.

Durbin, T. J. (1978), Calibration of a mathematical model of the Antelope Valley groundwater basin, California, *Water Supply Pap.*, *2046*, 51 pp., U.S. Geol. Surv., Reston, VA.

Eberhart-Phillips, D., and A. J. Michael (1993), Three-dimensional velocity structure, seismicity, and fault structure in the Parkfield region, Central California, *J. Geophys. Res.*, *98*(B9), 15737-15758, doi: 10.1029/93JB01029.

Erkan, K., and D. D. Blackwell (2008), A thermal test of the post-subduction tectonic evolution along the California transform margin, *Geophys. Res. Lett.*, *35*(7), L07309, doi: 10.1029/2008GL033479.

Evans, J. P., C. B. Forster, and J. V. Goddard (1997), Permeability of fault-related rocks, and implications for hydraulic structure of fault zones, *J. Struct. Geol.*, *19*(11), 1393-

1404.

Evans, J. P., K. E. Bradbury, S. D. Draper, D. C. Barton, and J. G. Solum (2007), Mineralogic and textural analyses of fault-related rocks at depth; analysis of SAFOD rocks and the top of the seismogenic zone, *Geol. Soc. Am. Abstracts with Programs*, *39*(6), 375.

Faulkner, D. R. (2004), A model for the variation in permeability of clay-bearing fault gouge with depth in the brittle crust, *Geophys. Res. Lett.*, *31*(19), L19611, doi: 10.1029 /2004GL020736.

Freeze, R. A., and P. A. Witherspoon (1967), Theoretical analysis of regional groundwater flow; [Part 2], Effect of water-table configuration and subsurface permeability variation, *Water Resour. Res.*, *3*(2), 623-634, doi: 10.1029/ WR003 i002p00623.

Fuis, G. S., T. Ryberg, N. J. Godfrey, D. A. Okaya, and J. M. Murphy (2001a), Crustal structure and tectonics from the Los Angeles Basin to the Mojave Desert, Southern California, *Geology*, *29*(1), 15-18.

Fuis, G. S., T. Ryberg, W. J. Lutter, and P. L. Ehlig (2001b), Seismic mapping of shallow fault zones in the San Gabriel Mountains from the Los Angeles region seismic experiment, Southern California, *J. Geophys. Res.*, 106(B4), 6549-6568, doi: 10.1029/ 2000JB900189.

Fulton, P. M., and D. M. Saffer (2009), The effect of thermal refraction on heat flow scatter near the San Andreas Fault, Parkfield, CA, *J. Geophys. Res.*, *114*(B6), B06408.

Fulton, P. M., D. M. Saffer, R. N. Harris, and B. A. Bekins (2004), Re-evaluation of heat flow data near Parkfield, CA; evidence for a weak San Andreas Fault, *Geophys. Res. Lett.*, *31*(15), L15S15, doi: 10.1029/2003GL019378.

Fulton, P. M., D. M. Saffer, and B. A. Bekins (2009), A critical evaluation of crustal dehydration as the cause of an overpressured and weak San Andreas Fault, *Earth Planet. Sci. Lett.*, *284*(3-4), 447-454, doi:10.1016/j.epsl.2009.05.009.

Furlong, K. P., and S. Y. Schwartz (2004), Influence of the Mendocino triple junction on the tectonics of coastal California, *Annu. Rev. Earth Pl. Sc.*, *32*, 403-433, doi: 10.1146/annurev.earth.32.101802.120252.

Furlong, K. P., J. Lock, C. Guzofski, J. Whitlock, and H. M. Benz (2003), The Mendocino crustal conveyor; making and breaking the California crust, *Int. Geol. Rev.*, *45*(9), 767-779.

Galehouse, J. S. (1967), Provenance and paleocurrents of the Paso Robles Formation, California, *Geol. Soc. Am. Bull.*, *78*(8), 951-978, doi: 10.1130/0016-7606(1967)78[951:PAPOTP]2.0.CO;2.

Galushkin, Y. I., A. A. Shreider, A. A. Bulychev, and A. A. Shreider (2006), Heat flow and thermal evolution of the lithosphere of the Black Sea Basin, *Oceanology*, *46*(2), 296-314, doi: 10.1134/S0001437006020147.

Goes, S., R. Govers, S. Y. Schwartz, and K. P. Furlong (1997), Three-dimensional thermal modeling for the Mendocino triple junction area, *Earth Planetary Sci. Lett.*, *148*(1-2), 45-57.

Griscom, A., and R. C. Jachens (1990), Tectonic implications of gravity and magnetic models along east-west seismic profiles across the Great Valley near Coalinga Coalinga, in *The Coalinga, California, earthquake of May 2, 1983*, edited by M. J. Rymer and W. L. Ellsworth, *U.S. Geol. Surv. Prof. Pap.*, 1487, 69-78.

Guzofski, C. A., and K. P. Furlong (2002), Migration of the Mendocino triple junction and ephemeral crustal deformation; implications for California Coast Range heat flow, *Geophys. Res. Lett.*, *29*(1), 1012, doi: 10.1029/2001GL013614.

Guzofski, C. A., J. H. Shaw, G. Lin, and P. M. Shearer (2007), Seismically active wedge structure beneath the Coalinga Anticline, San Joaquin Basin, California, *J. Geophys. Res.*, *112*(B3), B03S05, doi: 10.1029/2006JB004465.

Hammond, D. E., B. W. Leslie, T. L. Ku, and T. Torgersen (1988), ^{222}Rn concentrations in deep formation waters and the geohydrology of the Cajon Pass borehole, *Geophys. Res. Lett.*, 15(9), 1045-1048, doi: 10.1029/GL015i009p01045.

Hardebeck, J. L., and E. Hauksson (1999), Role of fluids in faulting inferred from stress field signatures, *Science*, *285*(5425), 236-239.

Harmsen, F. J., and R. D. Merrill (1988), Pliocene storm-influenced tidal deposits; last phases of marine sedimentation in the northwestern San Joaquin Basin, *Geol. Soc. Am. Abstracts with Programs*, *20*(3), 167.

Henry, S. G., and H. N. Pollack (1988), Terrestrial heat flow above the Andean subduction Zone in Bolivia and Peru, *J. Geophys. Res.*, *93*(B12), 15153-15162, doi: 10.1029/JB093iB12p15153.

Henyey, T. L., and G. J. Wasserburg (1971), Heat flow near major strike-slip faults in California, *J. Geophys. Res.*, *76*(32), 7924-7946.

Hole, J. A., T. Ryberg, G. S. Fuis, F. Bleibinhaus, and A. K. Sharma (2006), Structure of the San Andreas fault zone at SAFOD from a seismic refraction survey, *Geophys. Res. Lett.*, 33(7), L07312, doi: 10.1029/2005GL025194.

Ikari, M. J., D. M. Saffer, and C. Marone (2009), Frictional and hydrologic properties of clay-rich fault gouge, *J. Geophys. Res.*, *114*, B05409, doi: 10.1029/2008JB006089.

Irwin, W. P., and I. Barnes (1975), Effect of geologic structure and metamorphic fluids on seismic behavior of the San Andreas fault system in central and northern California, *Geology*, *13*(12), 713-716.

Izbicki, J. A., J. Radyk, and R. L. Michael (2000), Water movement through a thick unsaturated zone underlying an intermittent stream in the western Mojave Desert, Southern California, USA, *J Hydrol*, *238*(3-4), 194-217.

Izbicki, J. A., R. U. Johnson, J. Kulongoski, and S. Predmore (2007), Ground-water recharge from small intermittent streams in the western Mojave Desert, California, *Prof. Pap., 1703*, 26 pp., U.S. Geol. Surv., Reston, VA.

Jayko, A. S., M. C. Blake, Jr., and T. A. Harms (1987), Attenuation of the Coast Range Ophiolite by extensional faulting, and nature of the Coast Range "thrust," California, *Tectonics*, *6*(4), 475-488, doi: 10.1029/TC006i004p00475.

Jaupart, C., J. G. Sclater, and G. Simmons (1981), Heat flow studies; constraints on the distribution of uranium, thorium, and potassium in the continental crust, *Earth Planet. Sci. Lett.*, *52*(2), 328-344.

Jennings, C. W., R. G. Strand, and R. A. Rogers (1977), Geologic Map of California, scale 1:750,000, *California Geologic Data Map Series Map No. 2*, California Division of Mines and Geology, Sacramento, CA.

Johnson, M. J. (1980), Geology and ground water in North-central Santa Cruz County, California, *Water Resour. Invest.*, *PB-81 113 243*, 38 pp., U.S. Geol. Surv., Reston, VA.

Johnson, C. M., and J. R. O'Neil (1984), Triple junction magmatism; a geochemical study of Neogene volcanic rocks in western California, *Earth Planet. Sci. Lett.*, *71*(2), 241-263.

Jones, M. L., S. Nagihara, and M. A. Smith (2003), The regional geothermal heat flow regime of the north-central Gulf of Mexico continental slope, *Trans. Gulf Coast Assoc. Geol. Soc.*, *53*, 363-373.

Kharaka, Y. K., L. D. White, G. Ambats, and A. F. White (1988), Origin of subsurface water at Cajon Pass, California, *Geophys. Res. Lett.*, *15*(9), 1049-1052, doi: 10.1029/GL015i009p01049.

Kooi, H. (2008), Spatial variability in subsurface warming over the last three decades; insight from repeated borehole temperature measurements in The Netherlands, *Earth Planet. Sci. Lett.*, *270*(1-2), 86-94, doi: 10.1016/j.epsl.2008.03.015.

Lachenbruch, A. H., and J. H. Sass (1980), Heat flow and energetics of the San Andreas fault zone, *J. Geophys. Res.*, *85*(B11), 6185-6222, doi: 10.1029/JB085iB11p06185.

Link, M. H., K. P. Helmold, and W. T. Lo (1986), Geologic description of upper Miocene Chanac and lower Pliocene Etchegoin formations; Part 1, Depositional environments, reservoir characteristics, and petrology, Kern Front Field, California, *AAPG Bull.*, *70*(4), 471.

Liu, L., and M. D. Zoback (1997), Lithospheric strength and intraplate seismicity in the New Madrid seismic zone, *Tectonics*, *16*(4), 585-595, doi: 10.1029/97TC01467.

Londquist, C. J., D. L. Rewis, D. L. Galloway, and W. F. McCaffery (1993), Hydrogeology and land subsidence, Edwards Air Force Base, Antelope Valley, California, January 1989 – December 1991, *Water Resour. Invest.*, 93-4114, 74 pp., U.S. Geol. Surv., Reston, VA.

Lubis, R. F., Y. Sakura, and R. Delinom (2008), Groundwater recharge and discharge processes in the Jakarta groundwater basin, Indonesia, *Hydrogeol. J.*, *16*(5), 927-938, doi: 10.1007/s10040-008-0278-1.

Lutter, W. J., C. Thurber, and G. S. Fuis (1995), An image of the upper 5 km from inversion of first arrivals from the 1994 LARSE experiment: line 1 from Seal Beach to El Miraje Lake, *Eos Trans. AGU* 76(46), Fall Meeting Suppl., Abstract F348.

Lutter, W. J., G. S. Fuis, C. H. Thurber, and J. Murphy (1999), Tomographic images of the upper crust from the Los Angeles Basin to the Mojave Desert, California; results from the Los Angeles region seismic experiment, *J. Geophys. Res.*, *104*(B11), 25543-25565, doi: 10.1029/1999JB900188.

Mabey, D. R. (1960), Gravity study of the western Mojave Desert, California, *Prof. Pap.*, *316-317*, 51-89., U.S. Geol. Surv., Reston, VA.

Manning, C. E., and S. E. Ingebritsen (1999), Permeability of the continental crust; implications of geothermal data and metamorphic systems, *Rev. Geophys.*, *37*(1), 127-150, doi: 10.1029/1998RG900002.

Mansfield, C. F. (1979), Upper Mesozoic subsea fan deposits in the southern Diablo Range, California; record of the Sierra Nevada magmatic arc, *Geol. Soc. Am. Bull.*, *90*(11), 1025-1046.

Mase, C. W., J. H. Sass, A. H. Lachenbruch, and R. J. Munroe (1982), Preliminary heat-flow investigations of the California Cascades, *Open File Rep.*, *82-150*, 242 pp., U.S. Geol. Surv., Reston, VA.

McLean, H. (1981), Reservoir properties of submarine-fan facies; Great Valley Sequence, California, *J. Sediment. Res.*, *51*(3), 865-872, doi: 10.1306/212F7DC9-2B24-11D7-8648000102C1865D.

McPhee, D. K., R. C. Jachens, and C. M. Wentworth (2004), Crustal structure across the San Andreas Fault at the SAFOD site from potential field and geologic studies, *Geophys. Res. Lett.*, *31*(12), L12S03, doi: 10.1029/2003GL019363.

Montgomery, S. L., and M. F. Morea (2001), Antelope Shale (Monterey Formation), Buena Vista Hills Field; advanced reservoir characterization to evaluate CO_2 injection for enhanced oil recovery, *AAPG Bulletin*, *85*(4), 561-585, doi: 10.1306/8626C947-173B-11D7-8645000102C1865D.

Morrow, C. A., and J. D. Byerlee (1988), Permeability of rock samples from Cajon Pass, California, *Geophys. Res. Lett.*, *15*(9), 1033-1036, doi: 10.1029/GL015i009p01033.

Morrow, C.A., and Byerlee, J. D. (1992), Permeability of core samples from Cajon Pass scientific drill hole; results from 2100 to 3500 m depth, *J. Geophys. Res.*, *97*(B4), 5145-5151, doi: 10.1029/90JB00423.

Morrow, C. A., L. Q. Shi, and J. D. Byerlee (1981), Permeability and strength of San Andreas Fault gouge under high pressure, *Geophys. Res. Lett.*, *8*(4), 325-328, doi: 10.1029/GL008i004p00325.

Muir, K. S. (1972), Geology and ground water of the Pajaro Valley area, Santa Cruz and Monterey counties, California, *Open File Rep.*, *73-199*, 33 pp., U.S. Geol. Surv., Reston, VA.

Nissen, S. S., D. E. Hayes, Y. Bochu, Z. Weijun, C. Yongqin, and N. Xiaupin (1995), Gravity, heat flow, and seismic constraints on the processes of crustal extension; northern margin of the South China Sea, *J. Geophys. Res.*, *100*(B11), 22447-22483, doi: 10.1029/95JB01868.

Page, B. M., H. C. Wagner, D. S. McCulloch, E. A. Silver, and J. H. Spotts (1979), Tectonic interpretation of a geologic section of the continental margin off San Luis

Obispo, the southern Coast Ranges, and the San Joaquin Valley, California; cross-section summary, *Geol. Soc. Am. Bull.*, *90*(9), 808-812.

Page, B. M., G. A. Thompson, and R. G. Coleman (1998), Late Cenozoic tectonics of the central and southern Coast Ranges of California, *Geol. Soc. Am. Bull.*, *110*(7), 846-876, doi: 10.1130/0016-7606(1998) 110<0846: OLCTOT>2.3.CO;2.

Parizek, R. R., and K. A. Parizek (2005), Geothermal surveys used to map karst feeder channels, *Geol. Soc. Am. Abstracts with Programs*, *37*(7), 326.

Pellerin, C. L. M., and N. I. Christensen (1998), Interpretation of crustal seismic velocities in the San Gabriel – Mojave region, Southern California, *Tectonophysics*, *286*(1-4), 253-271.

Person, M., A. Banerjee, A. Hofstra, D. Sweetkind, and Y. Gao (2008), Hydrologic models of modern and fossil geothermal systems in the Great Basin; genetic implications for epithermal Au-Ag and carlin-type gold deposits, *Geosphere*, *4*(5), 888-917, doi: 10.1130/GES00150.1.

Powell, R. E., R. J. Weldon, II, and J. C. Matti (1993), The San Andreas Fault system; displacement, palinspastic reconstruction, and geologic evolution, *Geol. Soc. Am. Mem.*, *178*, 332 pp.

Rantz, S. E. (1969), Mean annual precipitation in the California region, *Open-File Map.*, U.S. Geol. Surv., Reston, VA.

Roeloffs, E. A. (1998), Persistent water level changes in a well near Parkfield, California, due to local and distant earthquakes, *J. Geophys. Res.*, *103*(B1), 869-889.

Roeloffs, E. A. (2001), Creep rate changes at Parkfield, California 1966-1999; seasonal, precipitation induced, and tectonic, *J. Geophys. Res.*, *106*(B8), 16525-16547, doi:

10.1029/2001JB000352.

Roeloffs, E. A., and E. Quilty (1997), Case 21; water level and strain changes preceding and following the August 4, 1985 Kettleman Hills, California, earthquake, *Pure Appl. Geophys.*, *149*(1), 21-60.

Rowland, J. C., M. Manga, and T. P. Rose (2008), The influence of poorly-interconnected fault zone paths on spring geochemistry, *Geofluids*, *8*(2), 93-101, doi: 10.1111/j.1468-8123.2008.00208.x.

Saar, M. O., and M. Manga (2004), Depth dependence of permeability in the Oregon Cascades inferred from hydrogeologic, thermal, seismic, and magmatic modeling constraints, *J. Geophys. Res.*, *109*(4), B04204, doi: 10.1029/2003JB002855.

Saffer, D. M., B. A. Bekins, and S. H. Hickman (2003), Topographically driven groundwater flow and the San Andreas heat flow paradox revisited, *J. Geophys. Res.*, *108*(B5), 2274, doi: 10.1029/2002JB001849.

Sass, J. H., A. H. Lachenbruch, S. P. Galanis, Jr., R. J. Munroe, and T. H. Moses, Jr. (1986), An analysis of thermal data from the vicinity of Cajon Pass, California, *Open File Rep.*, *86-0468*, 47 pp., U.S. Geol. Surv., Reston, VA.

Sass, J. H., A. H. Lachenbruch, T. H. Moses, Jr., and P. Morgan (1992), Heat flow from a scientific research well at Cajon Pass, California, *J. Geophys. Res.*, *97*(B4), 5017-5030, doi: 10.1029/91JB01504.

Sass, J. H., A. H. Lachenbruch, S. P. Galanis, Jr., P. Morgan, S. S. Priest, T. H. Moses, Jr., and R. J. Munroe (1994), Thermal regime of the southern Basin and Range Province; 1, Heat flow data from Arizona and the Mojave Desert of California and Nevada, *J. Geophys. Res.*, *99*(B11), 22093-22119, doi: 10.1029/94JB01891.

Sass, J. H., C. F. Williams, A. H. Lachenbruch, S. P. Galanis, Jr., and F. V. Grubb (1997), Thermal regime of the San Andreas Fault near Parkfield, California, *J. Geophys. Res.*, *102*(B12), 27575-27585, doi: 10.1029/JB102iB12p27575.

Scanlon, B. R. (1991), Evaluation of moisture flux from chloride data in desert soils, *J. Hydrol*, *128*(1-4), 137-156.

Scholz, C. H. (2000), Evidence for a strong San Andreas Fault, *Geology*, *28*(2), 163-166, doi: 10.1130/0091-7613(2000)028<0163:EFASSA>2.3.CO;2.

Sibson, R. H. (1982), Fault zone models, heat flow, and the depth distribution of earthquakes in the continental crust of the United States, *Bull. Seismol. Soc. Am.*, *72*(1), 151-163.

Silliman, S., and R. Robinson (1989), Identifying fracture interconnections between boreholes using natural temperature profiling; I, Conceptual basis, *Ground Water*, *27* (3), 393-402.

Sims, J. D. (1988), Geologic map of the San Andreas fault zone in the Cholame Valley and Cholame Hills quadrangles, San Luis Obispo and Monterey counties, California, *Miscellaneous Field Studies Map*, *MF-1995*, U.S. Geol. Surv., Reston, VA.

Sims, J. D. (1990), Geologic Map of the San Andreas Fault in the Parkfield 7.5-minute Quadrangle, Monterey and Fresno Counties, California, *Miscellaneous Field Studies Map*, *MF-2115*, U.S. Geol. Surv., Reston, VA.

Smith, L., and D. S. Chapman (1983), On the thermal effects of groundwater flow, *J. Geophys. Res.*, *88*(B1), 593-608, doi: 10.1029/JB088iB01p00593.

Smith, L., and D. S. Chapman (1985), The influence of water table configuration on the near-surface thermal regime, *J. Geodyn.*, *4*(1-4), 183-198.

Smith, L., C. Forster, and A. Woodbury (1989), Numerical simulation techniques for modeling advectively-disturbed thermal regimes, in *Hydrogeological Regimes and their Subsurface Thermal Effects*, edited by A. E. Beck, G. Garven, and L. Stegena, *Geophysical Monograph*, 47, 1-5.

Sneed, M., and D. L. Galloway (2000), Aquifer-system compaction and land subsidence; measurements, analyses, and simulations; the Holly Site, Edwards Air Force Base, Antelope Valley, California, *Water Resour. Invest.*, *00-4015*, 65 pp., U.S. Geol. Surv., Reston, VA.

Solum, J. G., S. H. Hickman, D. L. Kirschner, D. A. Lockner, D. Moore, and W. M. Calvin (2008), Large-scale continental deformation: fluid-rock interaction and compartmentalization along the San Andreas Fault at SAFOD, *Geol. Soc. Am. Abstracts with Program*, *40*(6), 274.

Stewart, R., and L. Peselnick (1977), Velocity of compressional waves in dry Franciscan rocks to 8 kbar and 300 degrees C, *J. Geophys. Res.*, *82*(14), 2027-2039, doi: 10.1029/ JB082i014p02027.

Thurber, C., S. Roecker, H. Zhang, S. Baher, and W. L. Ellsworth (2004), Fine-scale structure of the San Andreas fault zone and location of the SAFOD target earthquakes, *Geophys. Res. Lett.*, *31*(12), L09313, doi: 10.1029/2003GL019393.

United States Geological Survey, The National Map Seamless Server

United States Geological Survey, California Water Science Center

Unsworth, M., and P. A. Bedrosian (2004), Electrical resistivity structure at the SAFOD site from magnetotelluric exploration, *Geophys. Res. Lett.*, *31*(12), L12S05, doi: 10.10 29/2003GL019405.

Unsworth, M. J., P. E. Malin, G. D. Egbert, and J. R. Booker (1997), Internal structure of the San Andreas Fault at Parkfield, California, *Geology*, *25*(4), 359-362, doi: 10.1130/0091-7613(1997)025<0359:ISOTSA>2.3.CO;2.

Van Wijk, J. W., R. Govers, and K. P. Furlong (2001), Three-dimensional thermal modeling of the California upper mantle; a slab window vs. stalled slab, *Earth Planet. Sci. Lett.*, *186*(2), 175-186.

Voss, C. I. (1984), A finite-element simulation model for saturated-unsaturated, fluid-density-dependent ground-water flow with energy transport or chemically-reactive single-species solute transport, *Water Resour. Invest.*, *84-4369*, 409 pp., U.S. Geol. Surv., Reston, VA.

Waring, G. A. (1915), Springs of California, *Water Supply Pap.*, *0338*, 410 pp., U.S. Geol. Surv., Reston, VA.

Whittlesey, K. E., and D. J. Bottjer (1998), Pancho Rico Formation, Salinas Valley, CA; investigative stratigraphic and paleoecologic methods, *AAPG Bulletin*, *82*(5A), 862.

Wiersberg, T., and J. Erzinger (2007), A helium isotope cross-section study through the San Andreas Fault at seismogenic depths, *Geochemistry, Geophysics, Geosystems – G^3*, *8*(1), Q01002, doi: 10.1029/2006GC001388.

Williams, C. F., and T. N. Narasimhan (1989), Hydrogeologic constraints on heat flow along the San Andreas Fault; a testing of hypotheses, *Earth Planet. Sci. Lett.*, *92*(2), 131-143.

Williams, C.F., F. V. Grubb, and S. P. Galanis, Jr. (2004), Heat flow in the SAFOD pilot hole and implications for the strength of the San Andreas Fault, *Geophys. Res. Lett.*, *31*(15), L15S14, doi: 10.1029/2003GL019352.

Williams, C. F., S. P. Galanis, Jr., F. V. Grubb, and T. H. Moses, Jr. (1994), The thermal regime of Santa Maria Province, California, *Bull.*, *B 1995-F,G*, F1– F25, U.S. Geol. Surv., Reston, VA.

Wood, W. W., and W. E. Sanford (1995), Chemical and isotopic methods for quantifying ground-water recharge in a regional, semiarid environment, *Ground Water*, *33*(3), 458-468.

Wylie, A. S., Jr., D. H. Sturm, R. L. Gardiner, and M. F. Mercer (1996), Surface geology of the northern Midway-Sunset Field and adjacent Temblor Range, Kern County, California, *AAPG Annual Meeting Expanded Abstracts*, *5*, 154.

Yale, D. P. (1984), Network modelling of flow, storage, and deformation in porous rocks, Ph.D. Thesis, 182 pp., Stanford University, Stanford, CA.

Yang, Y., and A. C. Aplin (2007), Permeability and petrophysical properties of 30 natural mudstones, *J. Geophys. Res.*, *112*(B3), B03206, doi: 10.1029/2005JB004243.

Zhang, H., Y. Liu, C. Thurber, and S. Roecker (2007), Three-dimensional shear-wave splitting tomography in the Parkfield, California, region, *Geophys. Res. Lett.*, *34*(24), L24308, doi: 10.1029/2007GL031951.

Zoback, M. D. (1982), Measurements of In-Situ Stress, Fracture Distribution, Permeability, and Sonic Velocity, in Hydraulic Fracturing and Geothermal Energy, edited by S. Nemat-Nasser, H. Abé, and S. Hirakawa, 205-217, Martinus Nijhoff Publishers, The Hague, The Netherlands.

APPENDICES